
NON-INTRUSIVE REDUCED ORDER MODELING OF NATURAL CONVECTION IN POROUS MEDIA USING CONVOLUTIONAL AUTOENCODERS: COMPARISON WITH LINEAR SUBSPACE TECHNIQUES

A PREPRINT

Teeratrorn Kadeethum

Sibley School of Mechanical and Aerospace Engineering
Cornell University, New York, USA
tk658@cornell.edu

Francesco Ballarin

Department of Mathematics and Physics
Catholic University of the Sacred Heart, Brescia, Italy
francesco.ballarin@unicatt.it

Youngsoo Choi

Lawrence Livermore National Laboratory
California, USA
choi15@llnl.gov

Daniel O'Malley

Los Alamos National Laboratory
New Mexico, USA
omalled@lanl.gov

Hongkyu Yoon

Sandia National Laboratories
New Mexico, USA
hyoon@sandia.gov

Nikolaos Bouklas

Sibley School of Mechanical and Aerospace Engineering
& Center for Applied Mathematics
Cornell University, New York, USA
nb589@cornell.edu

July 30, 2021

ABSTRACT

Natural convection in porous media is a highly nonlinear multiphysical problem relevant to many engineering applications (e.g., the process of CO₂ sequestration). Here, we present a non-intrusive reduced order model of natural convection in porous media employing deep convolutional autoencoders for the compression and reconstruction and either radial basis function (RBF) interpolation or artificial neural networks (ANNs) for mapping parameters of partial differential equations (PDEs) on the corresponding nonlinear manifolds. To benchmark our approach, we also describe linear compression and reconstruction processes relying on proper orthogonal decomposition (POD) and ANNs. We present comprehensive comparisons among different models through three benchmark problems. The reduced order models, linear and nonlinear approaches, are much faster than the finite element model, obtaining a maximum speed-up of 7×10^6 because our framework is not bound by the Courant–Friedrichs–Lewy condition; hence, it could deliver quantities of interest at any given time contrary to the finite element model. Our model's accuracy still lies within a mean squared error of 0.07 (two-order of magnitude lower than the maximum value of the finite element results) in the worst-case scenario. We illustrate that, in specific settings, the nonlinear approach outperforms its linear counterpart and vice versa. We hypothesize that a visual comparison between principal component analysis (PCA) or t-Distributed Stochastic Neighbor Embedding (t-SNE) could indicate which method will perform better prior to employing any specific compression strategy.

Keywords natural convection · non-intrusive · data-driven · reduced order modeling · deep convolutional autoencoder · neural networks · finite element · nonlinear problem

1 Introduction

The problem of natural convection in porous media is involved in various engineering applications ranging from geothermal energy, seawater intrusion, contaminant transport to the storage of nuclear and radioactive waste [Taron and Elsworth, 2009, Nick et al., 2013, Zheng and Bennett, 2002, Rutqvist et al., 2005]. Typically, the problem behavior is characterized by the Rayleigh number (Ra), a dimensionless index indicating laminar or turbulent flow regimes. Additionally, an alteration in the fluid’s temperature or concentration resulting in variations in fluid density and viscosity (i.e., formation heterogeneity) could, in turn, influence the fluid flow field through fingering instabilities [Nield and Bejan, 2006]. One of many practical examples of interest is the process of carbon dioxide (CO_2) sequestration in aquifers. Depending on system Ra and the formation heterogeneity, convective mixing can greatly accelerate CO_2 dissolution during geologic carbon storage [Hassanzadeh et al., 2007, Neufeld et al., 2010].

To approximate the problem of natural convection in porous media, we utilize the mixed finite element method and interior penalty enriched Galerkin approximation for spatial discretization and the 4th-order backward differentiation formula for time-stepping as our full order model (FOM) as previously implemented by the authors [Kadeethum et al., 2021a]. This combination is selected to guarantee local mass conservation and accurately capture the gravity-driven flow in the advection-dominated regime [Zhang et al., 2016, Hosseini et al., 2020]. However, this FOM requires substantial computational resources because it is highly nonlinear and needs a very small time-step to satisfy Courant–Friedrichs–Lewy (CFL) condition [Diersch, 1988, Frolkovič and De Schepper, 2000, Cheng and Rabinovich, 2020, Kolditz et al., 1998]. Hence, it is not directly suitable to handle large-scale inverse problems, optimization, or control, in which an extensive set of simulations must be explored [Amsallem et al., 2015, McBane and Choi, 2021, Choi et al., 2019a, 2020a, Ballarin et al., 2019, Hansen, 2010, Hesthaven et al., 2016].

Alternatively, a reduced order model (ROM) has been developed to decrease computational cost while maintaining an acceptable accuracy, i.e., depending on applications, [Schilders et al., 2008, Schilders, 2008]. Recently, the ROM methodology has been applied to a range of parameterized problems (i.e., to repeated evaluations of a problem) depending on a set of parameters (μ), which could correspond to physical properties, geometric characteristics, or boundary conditions [Copeland et al., 2021, Hoang et al., 2020, Kim et al., 2020a, Choi et al., 2020b, Choi and Carlberg, 2019, Choi et al., 2021, Carlberg et al., 2018, Ballarin et al., 2019, Venturi et al., 2019, Hesthaven et al., 2016]. It is generally composed of two stages, (1) the offline and (2) online stages [Hesthaven et al., 2016]. The offline stage begins with initializing a set of input parameters, which we call a training set. Then the FOM is solved corresponding to each member in the training set (in the following, we will refer to the corresponding solutions as snapshots). Data compression techniques, which could be linear or nonlinear compression, are then used to compress FOM snapshots to produce basis functions that span a reduced (linear or nonlinear) space of very low dimensionality but still guarantee accurate reproduction of the snapshots [DeCaria et al., 2020, Cleary and Witten, 1984, Hijazi et al., 2020]. The ROM can then be solved during the online stage for any new value of μ by seeking an approximated solution in the reduced space.

For complex coupled processes a non-intrusive ROM is attractive because it does not require any cumbersome modifications of FOM source codes [e.g. Hoang et al., 2021, Xie et al., 2019, Xiao et al., 2019, Hesthaven and Ubbiali, 2018, Mignolet et al., 2013]. This alleviates several code compatibility complications since many of the source codes used to build FOMs may not be available or easily accessible, especially in legacy codes or commercial software [Xiao et al., 2015]. Consequently, the non-intrusive variants of ROM can provide more flexibility in coupling to any existing FOM platforms. We focus on two ways of building a ROM; the first path in, the linear approach, follows the recent development of Hesthaven and Ubbiali [2018], which has been adapted and applied to a wide range of problems [e.g. Girfoglio et al., 2020, Ortali et al., 2020, Demo et al., 2020, Gadalla et al., 2020, Kadeethum et al., 2021b]. This approach utilizes a set of reduced basis functions, which are linearly extracted from high-fidelity FOM solutions through proper orthogonal decomposition (POD). Then, the ROM solution, which belongs in a linear subspace of the solution manifold, is reconstructed from these reduced basis functions. In the second path, the nonlinear approach, we propose the compression of the high-fidelity FOM solutions through an autoencoder (AE in short) [e.g. Kim et al., 2020b,c, Phillips et al., 2020, Nikolopoulos et al., 2021, Lee and Carlberg, 2020, Fresca et al., 2021] learning a nonlinear manifold for the ROM solution. During the prediction phase, we reconstruct our ROM using nonlinear reconstruction (i.e., using a trained decoder to reconstruct our quantities of interest with a given nonlinear manifold). We want to emphasize that in contrast to the work presented in Kim et al. [2020b], Phillips et al. [2020], Lee and Carlberg [2020], our framework relies on the non-intrusive approach similar to Nikolopoulos et al. [2021], Fresca et al. [2021], which avoids any intrusive modifications of FOM source code. This type of non-intrusive approach for ROM using AE is termed Deep-Learning ROM (DL-ROM) by Fresca et al. [2021]. Hence, the framework could be easily extended to other engineering problems. This work has three main novelties

1. We propose a data-driven framework to approximate natural convection in porous media. The framework provides an online speed-up of $7 \times 10^3 - 7 \times 10^6$, depending on how many evaluations of the ROM are

required. As the framework stacks time-domains into the training set, it does not require a large number of training parameters μ to achieve the desired accuracy and avoid overfitting (see Remark 1 for more details). We also provide a comprehensive performance comparison between linear and nonlinear compression and reconstruction techniques.

2. The framework can handle data provided from FOM with adaptive time-stepping, which is essential for an advection-dominated problem (i.e., to satisfy CFL condition). The framework can also deliver the solution at any time, including times that do not exist in the training snapshots. This is an asset of our ROM because it is not bound by CFL conditions and can evaluate our quantities of interest at any timestamps that we require. For instance, we may be interested in a temperature field at one, two, and three hours with given Ra value. To achieve that using FOM, you may need to go through many steps in between. However, through ROM, you only need to evaluate it at those three times.
3. We provide a qualitative way to select between linear and nonlinear approaches using latent space visualization. We note that even though governing equations remain the same throughout this study, the linear approach might be a better choice than its nonlinear counterpart and vice-versa depending on geometry and boundary conditions.

The rest of the manuscript is summarized as follows. We begin with the model description and corresponding governing equations in Section 2. The presentation of the discretization of the natural convection problem and its solver could be found in appendix A. The two variants of the ROM framework following the linear and nonlinear approaches are discussed in Section 3. We then illustrate our ROM framework using three numerical examples in Section 4. We provide discussions on the ROM's performance, comparison between linear and nonlinear compression and reconstruction, and qualitative guidelines for selecting the subspace (between linear subspace and nonlinear manifold) in Section 5.

2 Problem description

This section briefly describes all the equations used in this study, namely mass balance and heat advection-diffusion equations. Let $\Omega \subset \mathbb{R}^d$ ($d \in \{1, 2, 3\}$) denote the computational domain and $\partial\Omega$ denote the boundary. \mathbf{X}^* are spatial coordinates in Ω , e.g. $\mathbf{X}^* = [x^*, y^*]$ when $d = 2$. The time domain is denoted by $\mathbb{T} = (0, \tau]$ with $\tau > 0$. Primary variables used in this paper are $\mathbf{u}^*(\cdot, t^*) : \Omega \times \mathbb{T} \rightarrow \mathbb{R}^d$, which is a vector-valued Darcy velocity (m/s), $p^*(\cdot, t^*) : \Omega \times \mathbb{T} \rightarrow \mathbb{R}$, which is a scalar-valued fluid pressure (Pa), and $T^*(\cdot, t^*) : \Omega \times \mathbb{T} \rightarrow \mathbb{R}$, which is a scalar-valued fluid temperature (C). Time is denoted as t^* (s).

Applying the Boussinesq approximation [Joseph, 2013] to the mass balance equations results in the density difference only appearing in the buoyancy term. The mass balance equations are

$$\mathbf{u}^* + \kappa (\nabla p^* + \mathbf{y} (\rho - \rho_0) g) = 0, \quad (1)$$

and

$$\nabla \cdot \mathbf{u}^* = 0, \quad (2)$$

where $\kappa = \mathbf{k}/\mu_f$ is the porous medium conductivity, μ_f is the fluid viscosity, \mathbf{y} is a unit vector in the direction of gravitational force, g is the constant acceleration due to gravity, ρ and ρ_0 are the fluid density at current and initial states, respectively. In addition, \mathbf{k} is the matrix permeability tensor defined as

$$\mathbf{k} := \begin{bmatrix} k_{xx} & k_{xy} \\ k_{yx} & k_{yy} \end{bmatrix}, \quad \text{if } d = 2, \quad (3)$$

Here, we only focus on 2D domain, $d = 2$, and simplify our problem by assuming \mathbf{k} is homogeneous and isotropic, which means $\mathbf{k} \rightarrow k$ and $\kappa \rightarrow \kappa$.

We assume that ρ is a linear function of T^* [Chen et al., 2006, Zhang et al., 2016] following

$$\rho = \rho_0 (1 - \alpha (T^* - T_0^*)), \quad (4)$$

where α is the thermal expansion coefficient, and T_0^* is the reference fluid temperature. We note that Equation (4) is the simplest approximation, and one may easily adapt the proposed method when employing a more complex relationship provided in Lake et al. [2014]. The heat advection-diffusion equation reads

$$\gamma \frac{\partial T^*}{\partial t^*} + \mathbf{u}^* \cdot \nabla T^* - K \nabla^2 T^* - f_c^* = 0. \quad (5)$$

Here, γ is the ratio between the porous medium heat capacity and the fluid heat capacity, K is the effective thermal conductivity, and f_c^* is a sink/source. We follow Nield and Bejan [2006] and define dimensionless variables as follows

$$\mathbf{X} := \frac{1}{H} \mathbf{X}^*, \quad t := \frac{\kappa}{\mu \gamma H^2} t^*, \quad p := \frac{\kappa}{K} p^*, \quad \mathbf{u} := \frac{H}{K} \mathbf{u}^*, \quad T := \frac{T^* - T_0^*}{\Delta T^*}, \quad f_c := \frac{t^*}{\Delta T^*} f_c^*, \quad (6)$$

where H is the dimensional layer depth, and ΔT^* is the temperature difference between two boundary layers. Consequently, we could rewrite our Equation (1) and Equation (2) using the dimensionless variables as

$$\begin{aligned} \mathbf{u} + \nabla p - \text{Ra} T &= 0, & \text{in } \Omega \times \mathbb{T}, \\ \nabla \cdot \mathbf{u} &= 0, & \text{in } \Omega \times \mathbb{T}, \\ p &= p_D & \text{on } \partial\Omega_p \times \mathbb{T}, \\ \mathbf{u} \cdot \mathbf{n} &= q_D & \text{on } \partial\Omega_q \times \mathbb{T}, \\ p &= p_0 & \text{in } \Omega \text{ at } t = 0, \end{aligned} \quad (7)$$

where $\partial\Omega_p$ and $\partial\Omega_q$ are the pressure and flux boundaries, respectively, and Ra is the Rayleigh number defined as

$$\text{Ra} := \frac{g \alpha \kappa \Delta T^* H}{K}. \quad (8)$$

We then write Equation (5) in dimensionless form as

$$\begin{aligned} \frac{\partial T}{\partial t} + \mathbf{u} \cdot \nabla T - \nabla^2 T - f_c &= 0, & \text{in } \Omega \times (0, \mathbb{T}], \\ T &= T_D & \text{on } \partial\Omega_T \times (0, \mathbb{T}], \\ (-\mathbf{u}T + \nabla T) \cdot \mathbf{n} &= T_{\text{in}} \mathbf{u} \cdot \mathbf{n} & \text{on } \partial\Omega_{\text{in}} \times (0, \mathbb{T}], \\ \nabla T \cdot \mathbf{n} &= 0 & \text{on } \partial\Omega_{\text{out}} \times (0, \mathbb{T}], \\ T &= T_0 & \text{in } \Omega \text{ at } t = 0, \end{aligned} \quad (9)$$

where $\partial\Omega_T$ is temperature boundary, $\partial\Omega_{\text{in}}$ and $\partial\Omega_{\text{out}}$ denote inflow and outflow boundaries, respectively, which are defined as

$$\partial\Omega_{\text{in}} := \{\mathbf{X} \in \partial\Omega : \mathbf{u} \cdot \mathbf{n} < 0\} \quad \text{and} \quad \partial\Omega_{\text{out}} := \{\mathbf{X} \in \partial\Omega : \mathbf{u} \cdot \mathbf{n} \geq 0\}. \quad (10)$$

The detail of discretization could be found in appendix A.

3 Non-intrusive reduced order model

The finite element solution scheme described in appendix A is typically a time-consuming operation, making it impractical to query such a solver in a real-time context whenever parametric studies are carried out. Such parametric studies are often of interest to account for uncertain material properties of porous media. Therefore in this work, we propose to employ a reduced order modeling strategy. A graphical summary of the paradigm is presented in Figure 1: the computations are divided into an offline phase for the ROM construction, which we will show through four consecutive main steps and (single-step) online stage for the ROM evaluation.

The first step of the offline stage (blue) represents an initialization of a training set (μ) of parameters used to train the framework, of cardinality M . Let $\mathbb{P} \subset \mathbb{R}^P$, $P \in \mathbb{N}$, be a compact set representing the range of variation of the

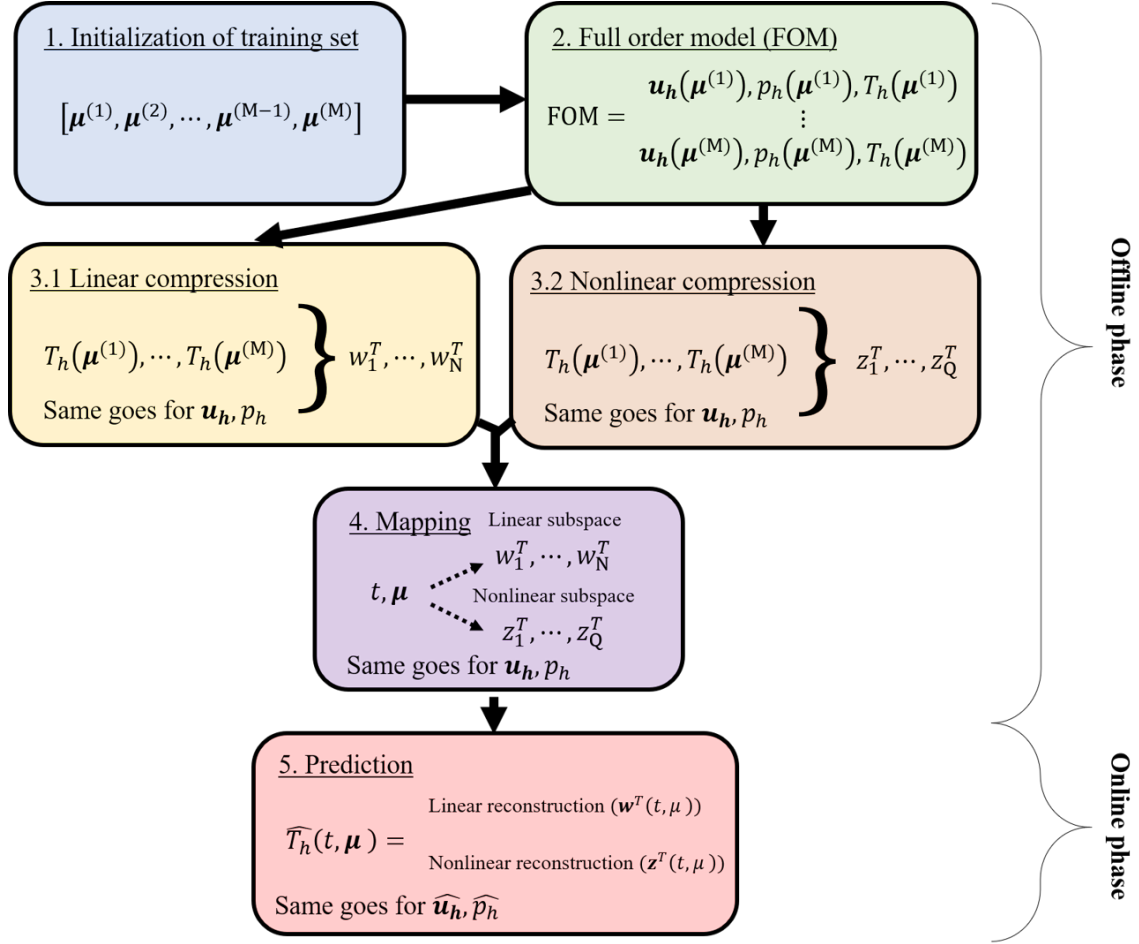


Figure 1: Summary of data-driven model reduction framework for natural convection in porous media.

parameters $\mu \in \mathbb{P}$. For the sake of notation we denote by $\mu_p, p = 1, \dots, P$, the p -th component of μ . To explore the parametric dependence of the phenomena, we define a discrete training set of M parameter instances. Each parameter instance in the training set will be indicated with the notation $\mu^{(i)}$, for $i = 1, \dots, M$. Thus, the p -th component of the i -th parameter instance in the training set is denoted by $\mu_p^{(i)}$ in the following. The choice of the value of M , as well as the sampling procedure from the range \mathbb{P} , is typically user- and problem-dependent. In this work, we use an equispaced distribution for the training set as done in Kadeethum et al. [2021b]. We note that adaptive sampling approaches could be employed and might result in a better model accuracy with a lower number of training instances [Paul-Dubois-Taine and Amsallem, 2015, Vasile et al., 2013, Choi et al., 2020a].

In the second step (green), we query the full order model (FOM), based on the finite element solver discussed in appendix A, for each parameter μ in the training set. After the second step, we have M snapshots of FOM results associated with the different parametric configurations in μ . Since the problem formulation is time-dependent, the output of the FOM solver for each parameter instance $\mu^{(i)}$ collects the time series representing the time evolution of the primary variables for each time-step t . Thus, each snapshot contains approximations of the primary variables (u_h, p_h , and T_h) at each time-step of the partition of the time domain \mathbb{T} . Therefore, based on the training set cardinality M and the number N^t of time-steps, we have a total of $N^t M$ training data to be employed in the subsequent steps. We note that as our finite element solver utilizes an adaptive time-stepping as presented in Equation (A.4), each snapshot may well have a different number of time-steps N^t , i.e. $N^t = N^t(\mu)$.

The third step aims to compress the information provided by the snapshots through either linear (yellow) or nonlinear (orange) compression. The linear compression employs the proper orthogonal decomposition (POD) technique [Hesthaven and Ubbiali, 2018, Willcox and Peraire, 2002, Choi et al., 2020b]. POD is used to determine characteristic spatial modes based on relative energy content criteria [Chatterjee, 2000, Liang et al., 2002, Wang et al., 2018]. During

the linear compression, only the first N modes are retained [Hesthaven et al., 2016], and employed as basis functions for the reduced basis spaces \mathcal{U}_N , \mathcal{P}_N , \mathcal{T}_N , used for approximating the velocity, pressure, and temperature fields respectively. The goal is to achieve $N \ll MN^t$ as well as $N \ll N_h^u$, $N \ll N_h^p$, and $N \ll N_h^T$. The resulting spatial modes, denoted by w_1^u, \dots, w_N^u , w_1^p, \dots, w_N^p , and w_1^T, \dots, w_N^T span a linear subspace of the velocity, pressure, and temperature fields respectively.

For the nonlinear compression, we utilize a deep convolutional autoencoder. The z_1^u, \dots, z_Q^u , z_1^p, \dots, z_Q^p , and z_1^T, \dots, z_Q^T represent the nonlinear manifold (also referred to as nonlinear manifolds) of the velocity, pressure, and temperature fields respectively. More details for z will be presented in Section 3.2. Again, our goal is to achieve $Q \ll MN^t$. Autoencoders could be considered as a nonlinear variation of POD [Romero et al., 2017, Baldi, 2012, Hinton and Zemel, 1994] and have been recently used in physics-based modeling [Kim et al., 2020b, Phillips et al., 2020, O'Malley et al., 2019, Goh et al., 2019]. They use the so-called *bottleneck* inside their hidden layers to force the networks to identify a reduced representation z of the training examples [Hinton and Zemel, 1994, Gehring et al., 2013]. We will discuss these linear and nonlinear compression approaches in detail in the following sections.

Next, for the fourth step (purple), for each snapshot, we map t and μ to its representation in the linear and nonlinear manifolds equivalently. This operation produces mappings between each pair (t, μ) , with $t \in \{t^0, \dots, t^{N^t}\}$ (N^t is different for each μ) and μ in the training set, and the best approximation in the reduced space \mathcal{U}_N , \mathcal{P}_N , \mathcal{T}_N for $u_h(\mu)$, $p_h(\mu)$, and $T_h(\mu)$ at time t , respectively. We note that the notion of *best approximation* is different between linear subspaces and nonlinear manifolds, and it will be discussed in the following sections. Finally, during the online phase (red), for given values of the parameter time instance t and μ , we aim to recover the online approximation to our primary variables by querying the corresponding reduced subspace and reconstructing the resulting finite element representation.

3.1 Linear approach

We provide a graphical illustration of procedures taken in the linear compression approach in Figure 2. We note that as steps 1 and 2 of our data-driven framework shown in Figure 1 are similar for both linear and nonlinear compression approaches, we here begin our procedure at the third step. Moreover, for the sake of compactness, we will focus on an expression and operation carried out for the temperature field T_h for the rest of this section. A very similar procedure is similarly carried out for the velocity field u_h and the pressure field p_h as well.

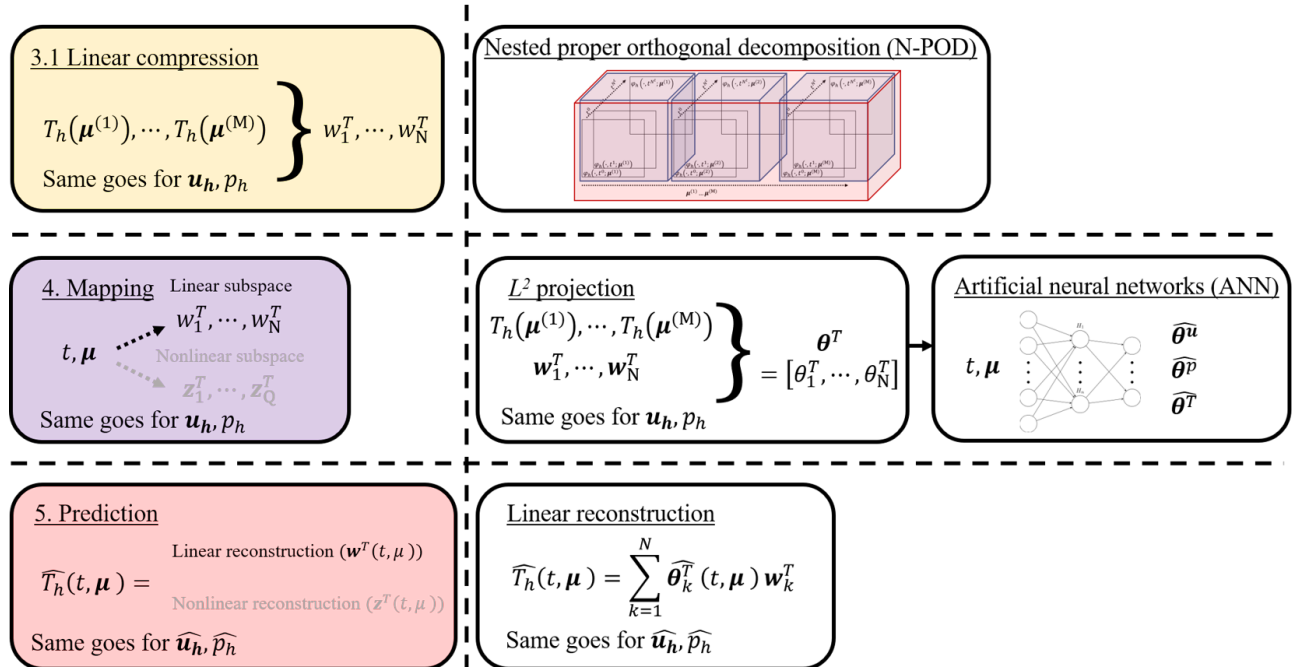


Figure 2: Procedures taken in linear compression approach. Note that step 1 and 2 are presented in Figure 1. We note that the nested POD technique compresses t (blue cubes) and μ (red cube), consecutively.

We have two main approaches to perform POD: (1) the *standard* POD method, in which all domains, t and μ , are compressed simultaneously (2) the *nested* POD technique, in which t and μ domains are compressed consecutively. In

this work, we employ the latter since our N^t is large (i.e., small-time-steps to satisfy Courant–Friedrichs–Lewy (CFL) condition, see Equation (A.4)). Consequently, the SVD computation of the standard POD case may become unfeasible because it requires a large amount of resources, both in terms of CPU time and memory storage (i.e., the bottleneck is due to the simultaneous compression in t and μ). Moreover, from Kadeethum et al. [2021b], the nested POD could provide comparable accuracy to the standard POD. We note that, in the reduced order modeling community, the nested POD can be also referred to as two-level POD or hierarchical approximate POD [Audouze et al., 2009, Rapún and Vega, 2010, Audouze et al., 2013, Ballarin et al., 2016, Himpe et al., 2018, Wang et al., 2019, Jacquier et al., 2020]. The detail of *nested* POD could be found in Appendix B.

We then, in the fourth step, obtain the optimal representation of each snapshot in the reduced basis spaces by means of an L^2 projection. This operation defines a map between each pair (t, μ) , with $t \in \{t^0, \dots, t^{N^t}\}$ and μ in the training set, and a vector of coefficients $\theta^T(t, \mu)$ that characterize the best approximation in the reduced space \mathcal{T}_N for the temperature field $T_h(\mu)$ at time t .

Let $\{\mathbf{w}_1, \dots, \mathbf{w}_N\}$ denote the basis functions spanning \mathcal{T}_N . Given a time t^n in the discretization of the time interval \mathbb{T} and a parameter instance $\mu^{(i)}$ in the training set we can define the best approximation $\tilde{T}_h(\cdot; t^n, \mu^{(i)})$ to $T_h(\cdot; t^n, \mu^{(i)})$ in \mathcal{T}_N as

$$\tilde{T}_h(\cdot; t^n, \mu^{(i)}) = \sum_{k=1}^N \theta_k^T(t^n, \mu^{(i)}) \mathbf{w}_k \quad (11)$$

where the coefficients θ_j^T are solutions to the L^2 projection problem, which can be stated as: Given $T_h(\cdot; t^n, \mu^{(i)})$, find $\theta^T(t^n, \mu^{(i)}) = [\theta_1^T(t^n, \mu^{(i)}), \dots, \theta_N^T(t^n, \mu^{(i)})] \in \mathbb{R}^N$ such that:

$$\sum_{j=1}^N \theta_j^T(t, \mu) (\mathbf{w}_j, \mathbf{w}_k)_T = (T_h(\cdot; t^n, \mu^{(i)}), \mathbf{w}_k)_T, k = 1, \dots, N.$$

We note that this results in a linear system, which left-hand side $(\mathbf{w}_j, \mathbf{w}_k)_T$ can be easily precomputed and stored in a $N \times N$ matrix. However, the right-hand side can only be computed once the FOM solutions are available for the training set and corresponding time-steps. The next step is to generalize the computation of the coefficients of the ROM expansion for any (time, parameter) pair using artificial neural networks trained on the available data $\theta^T(t^n, \mu^{(i)})$.

We now define a map $\hat{\theta}^T(t, \mu)$ for any time t in the time interval \mathbb{T} and any value of the parameter μ by training artificial neural networks (ANN) to approximate $\theta^T(t, \mu)$ based on the training data points obtained by L^2 projection [Hesthaven and Ubbiali, 2018]. The neural networks are built on the PyTorch platform [Paszke et al., 2019]. For simplicity, our ANN has five hidden layers, and each layer has seven neurons. We use *tanh* as our activation function. A detailed discussion on these hyperparameters could be found in [Kadeethum et al., 2021b]. Here, we use a mean squared error ($\text{MSE}^{\theta, T}$) as the metric of our network loss function, defined as follows

$$\text{MSE}^{\theta, T} = \frac{1}{MN^t} \sum_{i=1}^M \sum_{k=0}^{N^t} \left| \hat{\theta}^T(t^k, \mu^{(i)}) - \theta^T(t^k, \mu^{(i)}) \right|^2. \quad (12)$$

To minimize Equation (12), we train the neural network by adjusting each neuron weight (W) and bias (b) using the adaptive moment estimation (ADAM) algorithm [Kingma and Ba, 2014]. Throughout this study, we use a batch size of 32, a learning rate of 0.001, a number of epoch of 10,000, and we normalize both our input and output to $[0, 1]$. To prevent our networks from overfitting behavior, we follow early stopping and generalized cross-validation criteria [Hesthaven and Ubbiali, 2018, Prechelt, 1998a,b]. Note that instead of literally stopping our training cycle, we only save the set of trained weight and bias to be used in the online phase when the current validation loss is lower than the lowest validation from all the previous training cycle. We note that we do not use the RBF regression in linear approach because we follow procedures proposed in [Hesthaven and Ubbiali, 2018].

During the online or prediction phase (fifth step), for each inquiry (i.e., a value of μ), we evaluate the ANN to obtain $\hat{\theta}^T(t, \mu)$ for each $t \in \{t^0, \dots, t^{N^t}\}$. Subsequently, we reconstruct $\hat{T}_h(\cdot; t, \mu)$ as

$$\hat{T}_h(\cdot; t, \mu) = \sum_{k=1}^N \hat{\theta}_k^T(t, \mu) \mathbf{w}_k, \quad (13)$$

We note that the reduced basis $\{\mathbf{w}_k\}_{k=1}^N$ is already constructed during the POD phase; hence, recovering the online solutions, requires to evaluate $\hat{\theta}_k^T(t, \mu)$ from the trained ANN (which is typically extremely fast), and subsequently,

perform a reconstruction using Equation (13) (which only requires a linear combination of finite element functions). As a result, one typically enjoys an inexpensive online phase for each inquiry.

3.2 Nonlinear approach

In Figure 3, we provide a graphical illustration of procedures considered in the nonlinear approach that we propose here. Again, as steps 1 and 2 of our data-driven framework shown in Figure 1 are similar for both the linear and nonlinear approaches, we here begin our procedure at the third step. The main difference between the linear and nonlinear approaches lie within the compression as well as the reconstruction tool. For linear compression we use POD and for the reconstruction we use the L_2 projection. For the nonlinear compression (of $T_h(\mu^{(1)}), \dots, T_h(\mu^{(M)})$) and reconstruction we utilize AE. More specifically, for the compression we utilize the encoder, whereas for the reconstruction we utilize the decoder of the AE. To reiterate, we note that $T_h(\mu^{(i)})$ represents T_h given $\mu^{(i)}$, belonging to the training set, evaluated at all space and time. The AE could be considered as a nonlinear variation of POD [Baldi, 2012, Hinton and Zemel, 1994, Vincent et al., 2008], and it uses the so-called *bottleneck* inside its hidden layers to force the networks to identify a nonlinear manifolds (z_1^T, \dots, z_Q^T) of the training examples [Hinton and Zemel, 1994, Gehring et al., 2013].

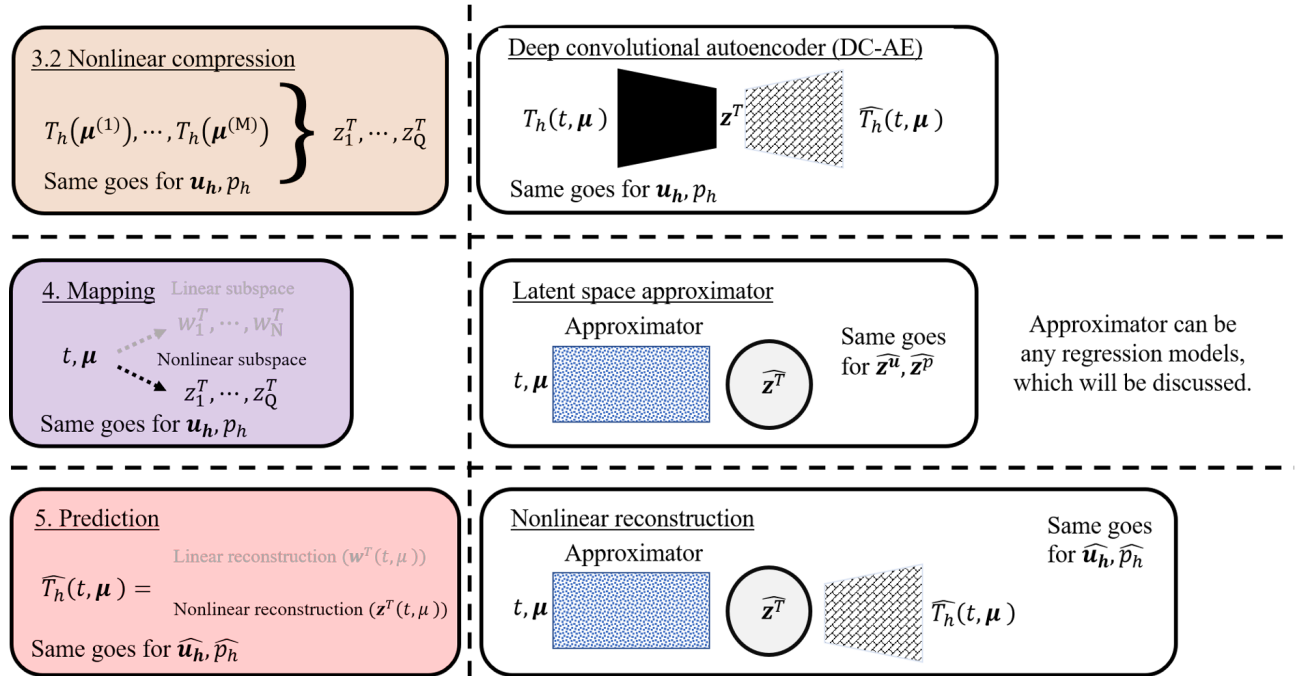


Figure 3: Procedures taken in nonlinear compression approach. Note that step 1 and 2 are presented in Figure 1.

The AE is composed of three main components: encoder, bottleneck, and decoder. The encoder task is to produce the nonlinear manifolds z^T with given T_h , i.e.

$$z^T(t, \mu) = \text{encoder}(T_h(t, \mu)), \quad \forall t \in \mathbb{T} \text{ and } \forall \mu \in \mathbb{P}. \quad (14)$$

This z^T lies within the bottleneck layers. The decoder then attempts to reconstruct \widehat{T}_h with given z^T , i.e.

$$\widehat{T}_h(t, \mu) = \text{decoder}(z^T(t, \mu)), \quad \forall t \in \mathbb{T} \text{ and } \forall \mu \in \mathbb{P}. \quad (15)$$

The encoder utilizes a contracting block that performs two convolutions followed by a max pool operation. The bottleneck employs two linear layers. The decoder uses expanding block in which it performs an upsampling and convolution of its two inputs. We note that each contracting block uses LeakyReLU with a negative slope of 0.2 as its activation function, and each expanding block uses ReLU as its activation function. Our model, in total, has seven contracting blocks and seven expanding blocks. We provide the detail of our AE in Appendix C.

We train our AE by minimizing

$$\text{MSE}^T = \frac{1}{MN^t} \sum_{i=1}^M \sum_{k=0}^{N^t} \left| \hat{T}_h \left(t^k, \boldsymbol{\mu}^{(i)} \right) - T_h \left(t^k, \boldsymbol{\mu}^{(i)} \right) \right|^2. \quad (16)$$

Here, we follow the training used in Kadeethum et al. [2021c]. We use the ADAM algorithm to adjust learnable parameters (W and b) [Kingma and Ba, 2014]. Throughout this study, we use $B = 32$ and a number of the epoch of 50. The learning rate (η) is calculated as [Loshchilov and Hutter, 2016]

$$\eta_c = \eta_{\min} + \frac{1}{2} (\eta_{\max} - \eta_{\min}) \left(1 + \cos \left(\frac{\text{step}_c}{\text{step}_f} \pi \right) \right) \quad (17)$$

where η_c is a learning rate at step step_c , η_{\min} is the minimum learning rate, which is set as 1×10^{-16} , η_{\max} is the maximum or initial learning rate, which is selected as 1×10^{-5} , step_c is the current step, and step_f is the final step. We note that each step refers to each time we perform back-propagation, including updating both encoder and decoder's parameters.

Following the training of the AE, we now establish the manifold $\mathbf{z}^T(t, \boldsymbol{\mu})$, $\forall t \in \mathbb{T}$ and $\forall \boldsymbol{\mu} \in \mathbb{P}$ during the fourth step shown in Figure 3. The data available for this task are the pairs $(t, \boldsymbol{\mu})$ in the training set. We achieve this through the training of a so-called *approximator*. In this study, we test three types of the approximators. The first one is ANN as also used in Section 3.1. To reiterate, our ANN has five hidden layers, and each layer has seven neurons. We use *tanh* as our activation function. Its loss function is

$$\text{MSE}^{\mathbf{z}^T} = \frac{1}{MN^t} \sum_{i=1}^M \sum_{k=0}^{N^t} \left| \hat{\mathbf{z}}^T \left(t^k, \boldsymbol{\mu}^{(i)} \right) - \mathbf{z}^T \left(t^k, \boldsymbol{\mu}^{(i)} \right) \right|^2. \quad (18)$$

Similar to Section 3.1, we use the ADAM algorithm to adjust each neuron W and b [Kingma and Ba, 2014], a batch size of 32, a learning rate of 0.001, a number of epoch of 10,000, and we normalize both our input $(t, \boldsymbol{\mu})$ and output (\mathbf{z}^T) to $[0, 1]$. We follow the same procedures presented in Section 3.1 to avoid over-fitting. The second and the third approximators are based on radial basis function (RBF) interpolation [Wright, 2003]. The second approximator uses a linear RBF, and the third one employs a cubic RBF. Similar to the ANN approximator, our input is $t, \boldsymbol{\mu}$, and our output is $\mathbf{z}^T(t, \boldsymbol{\mu})$. Please refer to Jones et al. [2001] for the detailed implementation.

During the online phase (the fifth step shown in Figure 3), we utilize the *trained* approximator and the *trained* decoder to approximate $\hat{T}_h(\cdot; t, \boldsymbol{\mu})$ for each inquiry (i.e., a value of $\boldsymbol{\mu}$) through

$$\hat{\mathbf{z}}^T(\cdot; t, \boldsymbol{\mu}) = \text{approximator}(t, \boldsymbol{\mu}), \quad (19)$$

and, subsequently,

$$\hat{T}_h(\cdot; t, \boldsymbol{\mu}) = \text{decoder}(\hat{\mathbf{z}}^T(\cdot; t, \boldsymbol{\mu})). \quad (20)$$

We note that each evaluation of approximator and decoder is extremely fast. Hence, one typically enjoys an inexpensive online phase for each inquiry.

Remark 1 *Our ROM does not require a large number of training parameters $\boldsymbol{\mu}$ to achieve the desired accuracy and avoid overfitting. We achieve this by stacking our time domain and parameter ($\boldsymbol{\mu}$) domain together during the training of AE. Consequently, the input to AE corresponds to not only each FEM results with given $\boldsymbol{\mu}$, but also each time-step. To elaborate, we refer to our Example 2; we have only 40 training values of $\boldsymbol{\mu}$, but our total input size to AE is 36110. By doing this, during our online inquiry, we simply interpolate at the time of interest within the time domain provided during the training phase.*

Remark 2 *We present the performance of the model that uses autoencoder without convolutional layers in appendix E. In summary, we observe that the model with convolutional layers (deep convolutional autoencoder) performs better.*

4 Numerical examples

We examine the performance of the proposed non-intrusive reduced order model following the nonlinear compression and reconstruction approach compared to the linear approach through three numerical examples. The information of each example is presented in Table 1. Throughout this section, for compactness, we will focus on the results of the temperature field. The velocity field and the pressure field results are similar to those of the temperature field. We note that M_v and M_t represent number of validation and testing sets, respectively. The parameters μ belonging to validation set and testing set are named $\mu_v^{(i)}$ and $\mu_t^{(i)}$, respectively.

As mentioned previously in Section 3, our FOM, see Appendix A, relies on unstructured grids. Our nonlinear compression and reconstruction, however, are applicable to a structured data set because they utilize convolutional layers. Hence, we interpolate the finite element result T_h to structured grids. We then replace the FOM dimension N_h^T , associated with the unstructured grid, with a pair $(\tilde{N}_h^T, \tilde{N}_h^T)$, associated to the structured grid. As we present in Table 1, the degrees of freedom or DOFs of the linear approach are less than those of the nonlinear approach.

Table 1: Summary of main information for each example.

	Example 1	Example 2	Example 3	remark
M	40	40	100	training set
M_v	10	10	20	validation set
M_t	10	10	20	test set
MN^t	16802	36110	86086	total training data
N^t range	[226, 477]	[790, 1010]	[740, 985]	for training, validation, and test sets
N_h^T	7110	9600	9600	DOFs: T_h
\tilde{N}_h^T	128×128	128×128	128×128	interpolated T_h on structured mesh
t range	[0.0, 0.1]	[0.0, 0.1]	[0.0, 0.1]	$[t^0, t^N]$
μ	Ra = [40, 80]	Ra = [350, 450]	Ra ₁ = [350, 450] Ra ₂ = [0.001, 100]	only Example 3 has two parameters

We present a summary of all geometries and boundary conditions we use in Figure 4. In short, Examples 1 and 2 represent cases that we have only one μ - Ra while Example 3 illustrates a case where we have two μ - Ra₁ and Ra₂. The detailed specification of each example will be discussed in the following subsections.

The summary of naming for each model is summarized in Table 2. They will be used in figures and discussion throughout the rest of this paper. Please refer to Sections 3, 3.1, and 3.2 for more detail on how we develop each model. In short, *linear* compression refers to the models that uses POD as a compression tool (see Section 3.1), and *nonlinear* compression refers to the models with AE as its compression tool (see Section 3.2). For the *linear* compression, subspace dimension refers to the number of reduced basis or N as well as the number of intermediate reduced basis or N_{int} . We assume $N = N_{int}$ for all models for simplicity. The subspace dimension is the number of latent space or Q for the *nonlinear* compression.

Table 2: Summary of naming for each model.

model name	compression	subspace dimension	approximator
POD 16 RB	linear	16	ANN
POD 50 RB	linear	50	ANN
POD 100 RB	linear	100	ANN
POD 500 RB	linear	500	ANN
AE 4 z: L-RBF	nonlinear	4	linear RBF
AE 4 z: C-RBF	nonlinear	4	cubic RBF
AE 4 z: ANN	nonlinear	4	ANN
AE 16 z: L-RBF	nonlinear	16	linear RBF
AE 16 z: C-RBF	nonlinear	16	cubic RBF
AE 16 z: ANN	nonlinear	16	ANN
AE 256 z: L-RBF	nonlinear	256	linear RBF
AE 256 z: C-RBF	nonlinear	256	cubic RBF
AE 256 z: ANN	nonlinear	256	ANN

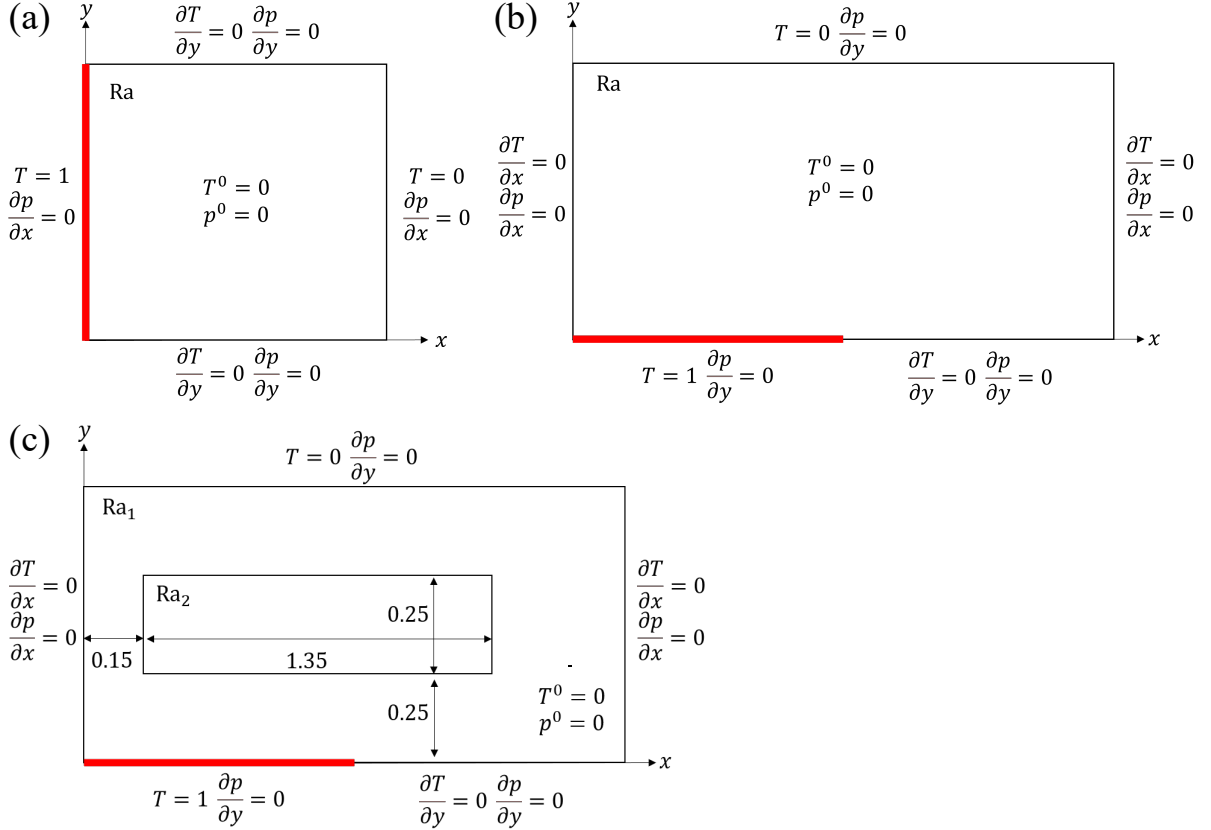


Figure 4: Domain and boundary conditions for (a) Example 1, (b) Example 2, and (c) Example 3. The red line indicates the region of the boundary where the temperature is elevated.

We note that FOM, POD, L_2 projection, RBF, and linear reconstruction are computed using AMD Ryzen Threadripper 3970X. The training of AE and ANN and nonlinear reconstruction are done by a single Quadro RTX 6000. We note that without using GPU, the training time of our AE is impractical. The training of ANN takes longer with CPU, but it is still able to finish within a reasonable time frame. A discussion of computational time will be provided in the discussion section (see Section 5).

4.1 Example 1: Heating from side problem

We adapt this example from Zhang et al. [2016]. The geometry and boundary conditions are shown in Figure 4a. The flow is driven by buoyancy as the fluid is heated on the left side of the domain. The fluid then flows upwards and rotates to the right side of the domain (see Figure 6a-c, first column). As presented in Table 1, we set $\mu = (\text{Ra})$, and its admissible range of variation is $[40.0, 80.0]$. We use $M = 40$, $M_v = 10$, $M_t = 10$ where M_v is a number of cases in validation set and M_t is a number of cases in test set. We have in total $MN^t = 16802$ training data points. Moreover, as our FOM utilizes the adaptive time-stepping, see Equation (A.4), the minimum and maximum N^t is 226 and 477, respectively.

We present the normalized eigenvalue as a function of the reduced basis for linear compression and AE validation loss during the training for nonlinear compression in Figure 5. We observe that by using $N_{\text{int}} = 50$, the POD could capture information similar to a case where we use $N_{\text{int}} = 100$. Moreover, the normalized eigenvalues of all cases decay reasonably fast, which may imply that the POD could capture most of the information with a small number of N_{int} and N . For the nonlinear compression, Figure 5b, the validation loss of all Q values is approximately 2×10^{-5} . This behavior implies that using only $Q = 4$; the AE could capture most of the information.

For the testing, we focus on a fixed realization of the uncertain parameter μ_t belonging to M_t , which is outside of the training set. To reiterate, we use $M_t = 10$. One example (out of 10) of the test cases is presented in Figure 6 for three

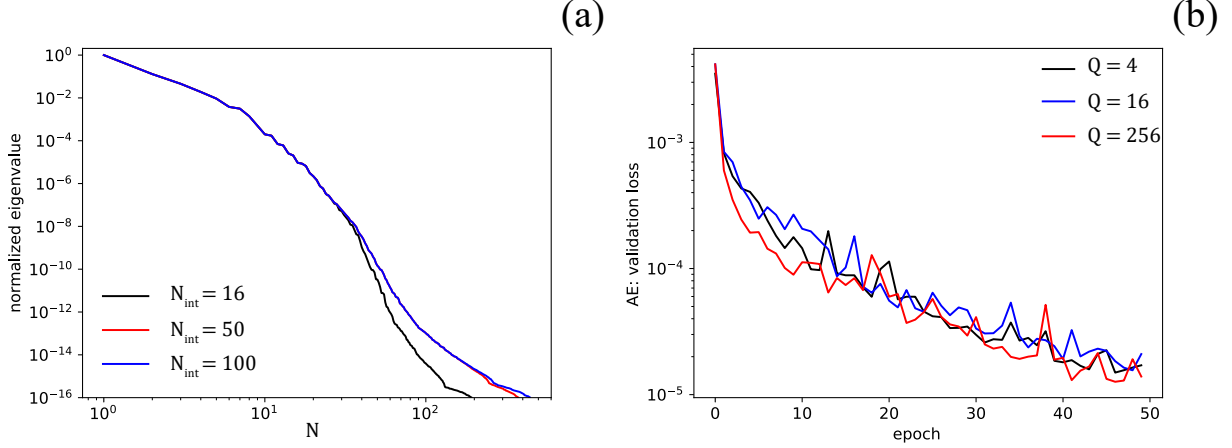


Figure 5: Example 1: (a) normalized eigenvalue as a function of reduced basis and (b) AE validation loss during the training.

different t values. In this figure, the difference between solutions produced by the FOM and ROM for both linear and nonlinear compression (further referred to as DIFF) is calculated by

$$\text{DIFF}_\varphi(t^k, \boldsymbol{\mu}_t^{(i)}) = \left| \varphi_h(\cdot; t^k, \boldsymbol{\mu}_t^{(i)}) - \widehat{\varphi}_h(\cdot; t^k, \boldsymbol{\mu}_t^{(i)}) \right|, \quad (21)$$

where φ_h is a finite-dimensional approximation of the set of primary variables corresponding to velocity, pressure, and temperature fields in this study (see appendix A). $\widehat{\varphi}_h$ is an approximation of φ_h produced by the ROM (either linear and nonlinear compression approaches). Thus, $\varphi_h(\cdot; t^k, \boldsymbol{\mu}_t^{(i)})$ and $\widehat{\varphi}_h(\cdot; t^k, \boldsymbol{\mu}_t^{(i)})$ represent φ_h and $\widehat{\varphi}_h$ at all space coordinates (i.e., evaluations at each DOF) at time t^k with input parameter $\boldsymbol{\mu}_t^{(i)}$, respectively. We note that, as mentioned at the beginning of Section 4, we here only present the results of the temperature field. Hence, φ_h and $\widehat{\varphi}_h$ represent T_h and \widehat{T}_h , respectively. From Figure 6, we observe that both linear and nonlinear compression (POD and AE, respectively) provide a reasonable approximation of the temperature field.

We then evaluate the performance of linear and nonlinear approaches by evaluating the mean square error ($\text{MSE}_\varphi(\cdot, \boldsymbol{\mu}_t^{(i)})$) and maximum DIFF (or $\max(\text{DIFF})$) of the test cases defined as follows

$$\text{MSE}_\varphi(\cdot, \boldsymbol{\mu}_t^{(i)}) := \frac{1}{N^t} \sum_{k=0}^{N^t} \left| \varphi_h(\cdot; t^k, \boldsymbol{\mu}_t^{(i)}) - \widehat{\varphi}_h(\cdot; t^k, \boldsymbol{\mu}_t^{(i)}) \right|_\varphi^2, \quad (22)$$

and

$$\max(\text{DIFF})_\varphi(\cdot, \boldsymbol{\mu}_t^{(i)}) := \left\| \text{DIFF}_\varphi(\cdot, \boldsymbol{\mu}_t^{(i)}) \right\|_\varphi^\infty. \quad (23)$$

We note that $\text{MSE}_\varphi(\cdot, \boldsymbol{\mu}_t^{(i)})$ and $\max(\text{DIFF})_\varphi(\cdot, \boldsymbol{\mu}_t^{(i)})$ represent the MSE and $\max(\text{DIFF})$ of all t for each $\boldsymbol{\mu}_t^{(i)}$. To reiterate, each $\boldsymbol{\mu}_t^{(i)}$ belongs to the testing set.

The box-plots of the MSE and $\max(\text{DIFF})$ for all $\boldsymbol{\mu}_t^{(i)}$ (testing set), are shown in Figure 7. From this figure, we observe that the linear approach (POD - as a compression tool) delivers a better accuracy than the proposed nonlinear approach. Moreover, as expected from the decay of eigenvalue shown in Figure 5, the model accuracy is not much different among the models with 16 RB, 50 RB, or 100 RB ($[\text{N}_{\text{int}} = 16, N = 16]$, $[\text{N}_{\text{int}} = 50, N = 50]$, or $[\text{N}_{\text{int}} = 100, N = 100]$, respectively). One observation is, for the linear approach, the error increases as the dimension of POD increases. This behavior occurs because there are two sources of errors. The first one is from the truncation of reduced basis (i.e., $N \leq M$), and the second one is the mapping between $(t, \boldsymbol{\mu})$ and linear subspace (\boldsymbol{w}) . Further detail and investigation could be found in Kadeethum et al. [2021b].

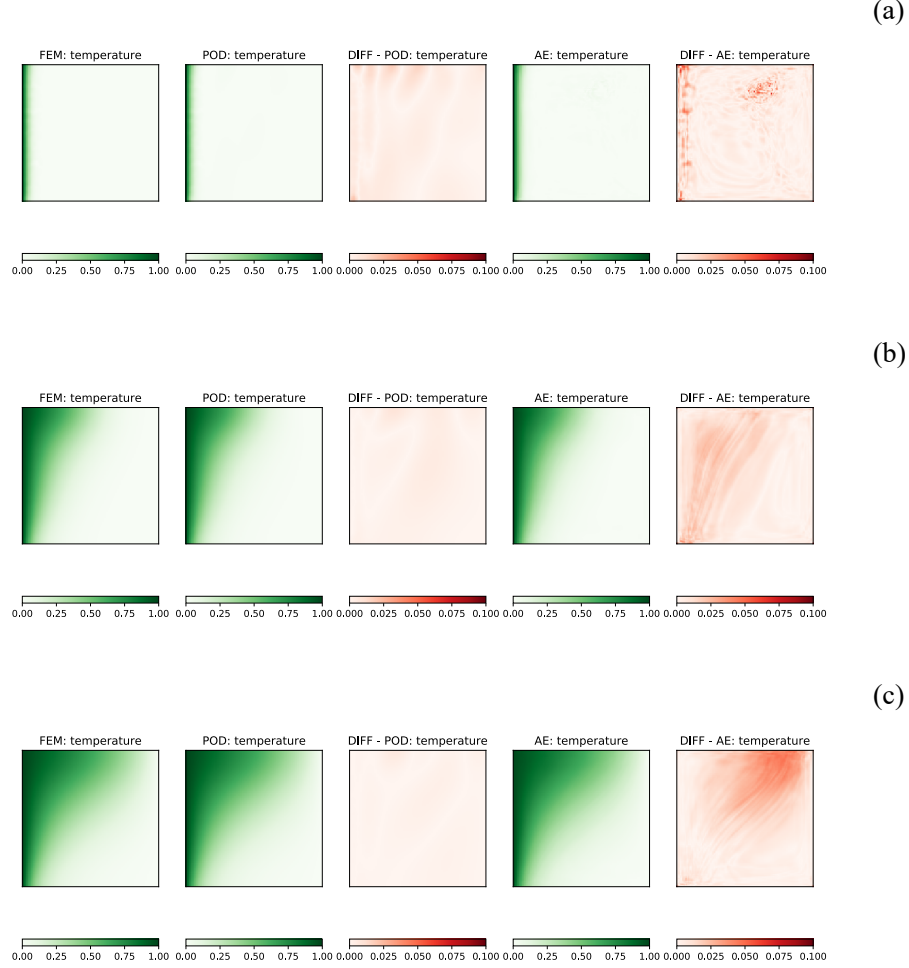


Figure 6: Example 1: test case ($Ra = 72.82$) results. (a) $t = 0.001$, (b) $t = 0.03$, and (c) $t = 0.07$. These results are produced by POD 16 RB and AE 16 z : ANN for POD: temperature and AE: temperature, respectively.

Among the nonlinear compression models, there is no obvious best choice. All models have the MSE results in the order of magnitude of 10^{-5} . The models that use ANN as the approximator to map (t, μ) to z (see Section 3.2 for more detail) seem to have a better performance on the MSE results than those that use RBF as their approximator. However, for the max(DIFF) results, the model with ANN approximator seems to be less accurate. Moreover, it is hard to conclude that by increasing the dimension of z , the framework's accuracy will be improved. We provide RBF training loss in Figure D.1 and ANN validation loss during the training in Figure D.3a.

The 50^{th} moving average of MSE as a function of t for Example 1 test set is presented in Figure 8. The MSE moving average of the linear compression, Figure 8a, gradually decreases and then abruptly increases toward the end of the simulation. The MSE moving average of the nonlinear compression, on the other hand, drops sharply at the beginning, then gradually picks up, and finally decreases again at the end of the simulation. We observe no clear relationship between the MSE values and Ra values.

4.2 Example 2: Elder problem

We progress to the Elder problem [Elder, 1967], which could be considered as a benchmark in the natural convection literature [Simpson and Clement, 2003]. The problem's domain and boundary conditions are presented in Figure 4b [Diersch and Kolditz, 2002, Zhang et al., 2016]. As the medium is heated at its lower part, the flow is driven upward by buoyancy. Again, see Table 1, we set $\mu = (Ra)$, and its admissible range of variation is $[350.0, 400.0]$. We note that as the Ra number considered in this case is relatively high, the flow instability may cause fingering behavior, see Figure

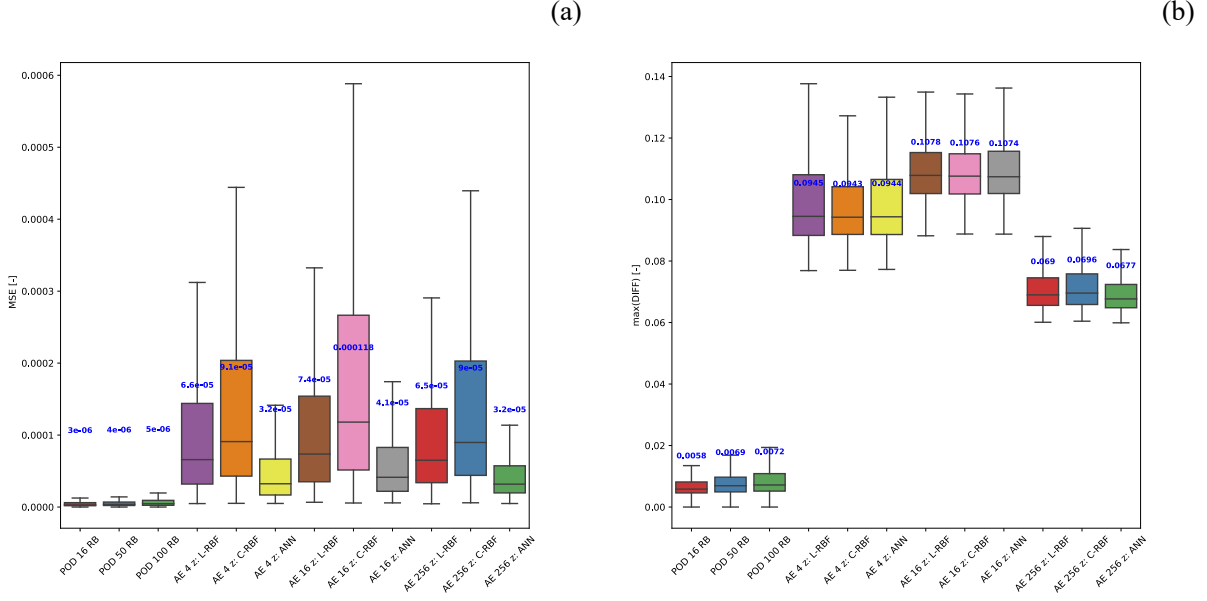


Figure 7: Example 1: Each model's performance on a test set (a) mean square error (MSE) and (b) maximum DIFF (max(DIFF)). Blue text represents a mean value. 16 RB, 50 RB, and 100 RB represent linear compression models with $[N_{\text{int}} = 16, N = 16]$, $[N_{\text{int}} = 50, N = 50]$, and $[N_{\text{int}} = 100, N = 100]$, respectively. The L-RBF and C-RBF are the nonlinear compression models with RBF with linear function and RBF with cubic function as its approximator, respectively.

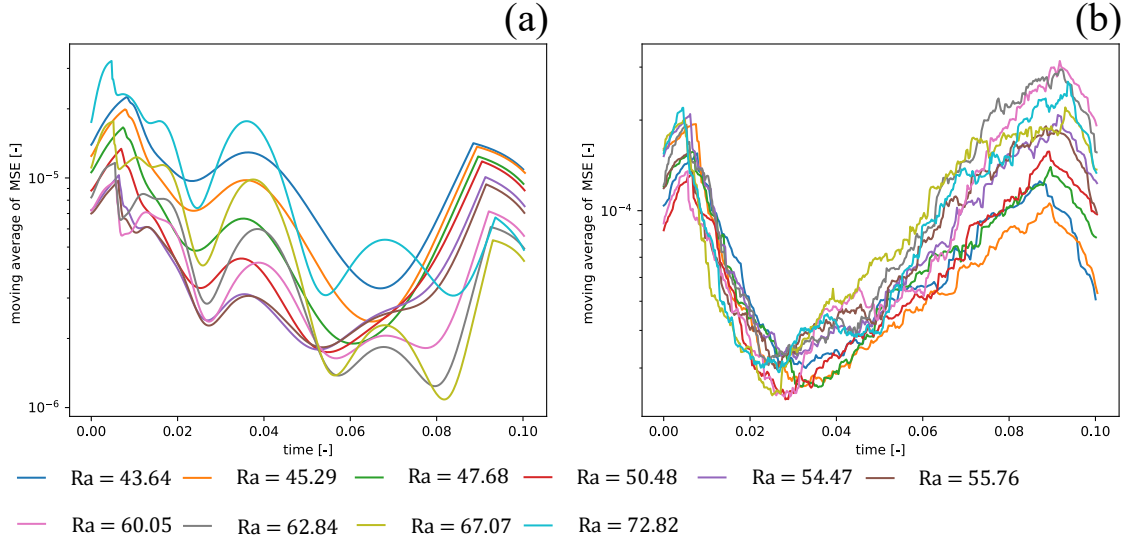


Figure 8: Example 1: 50th moving average of MSE on a test set of (a) POD 16 RB and (b) AE 16 z: ANN.

10a-c, first column, [Simpson and Clement, 2003, Zhang et al., 2016]. Moreover, the higher Ra value also affect the minimum and maximum N^t as its ranges is increased (compared with Example 1) to $[790, 1010]$. We use $M = 40$, $M_v = 10$, and $M_t = 10$. We have in total $MN^t = 36110$ training data points.

The normalized eigenvalue as a function of the reduced basis for the linear compression and AE validation loss for the nonlinear compression are presented in Figure 9. The eigenvalue decay behavior is different from Example 1. We observe that as N_{int} is increased, the POD requires more modes or N to capture information (i.e., the decay becomes slower as N_{int} grows). This behavior reflects that Example 2 is more challenging than Example 1 for the linear compression. For the nonlinear compression, Figure 9b, the validation loss of models with $Q \geq 16$ is approximately

2×10^{-6} , while the model with $Q = 4$ has the validation loss of 4×10^{-6} . This behavior implies that we may need to use the AE with at least 16 latent spaces to obtain better accuracy. We note that the AE validation loss of Example 2 is lower than that of Example 1 because we have more available training data points, see Table 1.

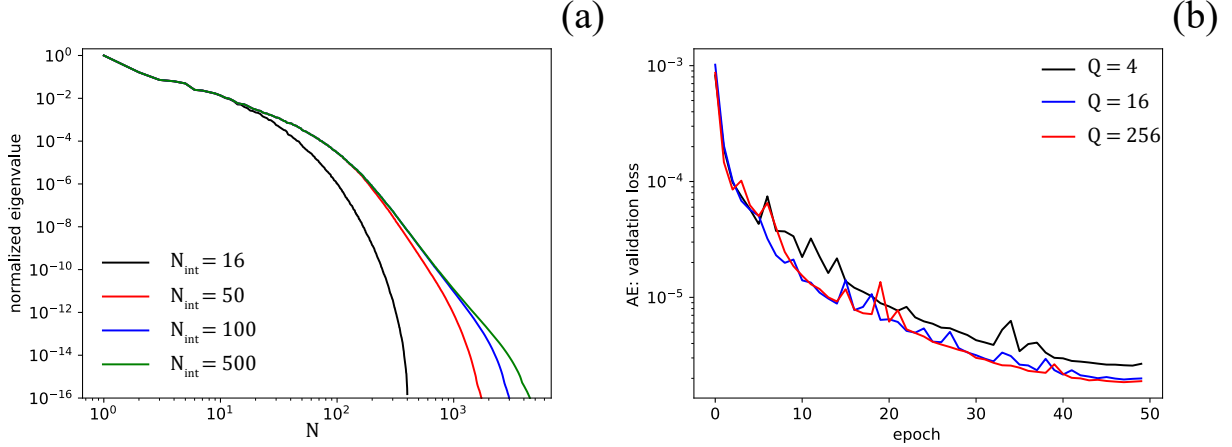


Figure 9: Example 2: (a) normalized eigenvalue as a function of reduced basis and (b) autoencoder validation loss during the training.

Similar to Example 1, we use $M_t = 10$. Again, we want to emphasize that our testing ($\mu_t^{(i)}$) set does not contain any μ values used in the training or validation set. One example (out of 10) of the test cases is presented in Figure 10 for three different t values. As expected and dissimilar to Example 1, we observe that the nonlinear compression provides a much better result than the linear compression, see DIFF values.

The MSE and max(DIFF) results of Example 2 are illustrated in Figure 11. From Figure 11a, the MSE values of the POD approach is approximately one order of magnitude higher than the AE with $Q = 4$, and two orders of magnitude higher than the nonlinear compression with $Q \geq 16$. The max(DIFF) results follow the same behavior of MSE results, see Figure 11b. We observe that there is no accuracy difference between the nonlinear compression with $Q = 16$ or $Q = 256$. Moreover, the nonlinear compression models with L-RBF, C-RBF, or ANN as its approximator have approximately the same accuracy. We provide RBF training loss in Figure D.2 and ANN validation loss during the training in Figure D.3b.

We also present the model's accuracy as a function of M in Figure 12, for $M = 5$, $M = 10$, and $M = 20$. For $M = 40$, please refer to Figure 11. Note that we only present results of nonlinear approach using $Q = 16$ with L-RBF, C-RBF, or ANN as its approximator. As expected, the model with higher M has a better accuracy, see Figures 11 and 12. The nonlinear models with $M \geq 10$ can deliver a better accuracy than those of the linear approach with $M = 40$.

We plot the 50^{th} moving average of MSE as a function of t in Figure 13. Unlike the previous example, see Figure 8, we could not find any patterns of MSE as a function of t in this plot. Moreover, as we also observe in Example 1, there is no clear relationship between the MSE values and Ra values.

4.3 Example 3: Modified Elder problem

So far, we have tested our framework on problems with only one parameter (i.e. μ is a 1-vector). In this example, we modify the Elder problem by inserting one subdomain as presented in Figure 4c. We add one more parameter and set $\mu = (Ra_1, Ra_2)$. Their admissible range of variation are $[350.0, 400.0]$ and $[0.001, 100.0]$ for Ra_1 and Ra_2 , respectively. Similar to the previous example, the range of Ra_1 may cause fingering behavior, see Figure 15a-c, first column. The minimum and maximum N^t is $[740, 985]$, which is not much different from Example 2. We use $M = 100$, $M_v = 20$, and $M_t = 20$. We have in total $MN^t = 86086$ training data points. Please refer to Table 1 for the summary.

We present the normalized eigenvalue as a function of reduced basis and AE validation loss during the training in Figure 14. As expected, the decay behavior of the eigenvalue (Figure 14a) is similar to that of Example 2, which means the decay becomes slower as N_{int} grows. This behavior shows that Examples 2 and 3 are more complex than Example 1. From Figure 14b, the nonlinear compression, the validation loss of model with $Q = 4$ is approximately 2×10^{-5} , model with $Q = 16$ is approximately 7×10^{-6} , and model with $Q = 256$ is approximately 6×10^{-6} . We note that the AE validation loss of Example 3 is higher than that of Example 1 even though we have more available training

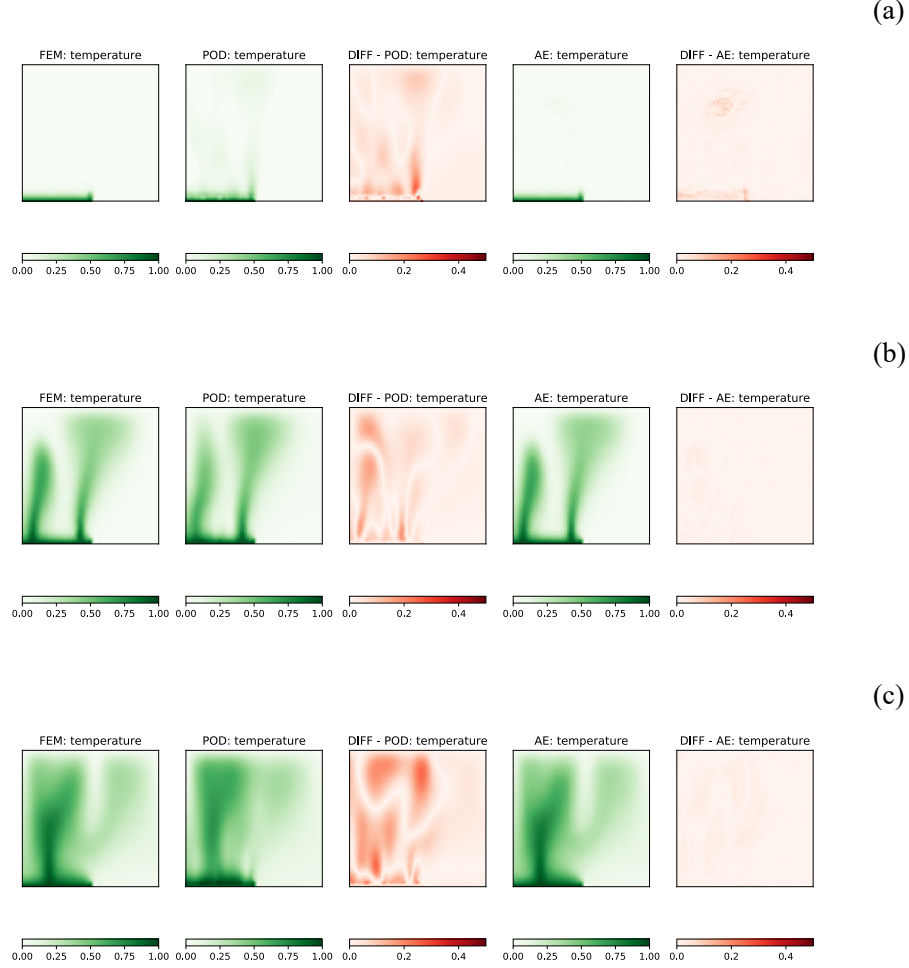


Figure 10: Example 2: test case ($Ra = 380.16$) results. (a) $t = 0.001$, (b) $t = 0.03$, and (c) $t = 0.07$. These results are produced by POD 16 RB and AE 16 z: ANN for POD: temperature and AE: temperature, respectively.

data points, see Table 1. However, the trend of the validation loss is still decreasing, which means it may require more epochs to achieve the same level of the validation loss.

In Example 3, we use $M_t = 20$, and we want to emphasize that our testing set ($\mu_t^{(i)}$) does not contain any μ values used in the training or validation set. One example (out of 20) of the test cases is presented in Figures 15 for three different t values. Similar to Example 2, we observe that the nonlinear compression provides a much better result than the linear compression, see DIFF values.

The MSE and max(DIFF) results of Example 3 are presented in Figure 16. We note that as we could not see much difference of the nonlinear compression models with RBF or ANN as their approximator (see Figures 7 and 11), we here present the results of the AE models with ANN approximator for the sake of compactness. The MSE values of the POD approach are approximately one order of magnitude higher than the AE with $Q = 4$ and almost two orders of magnitude higher than the nonlinear compression with $Q \geq 16$. From Figure 16b, the max(DIFF) results follow the same trend of the MSE results. Similar to Example 2, we observe no accuracy difference between the nonlinear compression with $Q = 16$ or $Q = 256$. We provide ANN validation loss during the training in Figure D.3c.

We present the 50^{th} moving average of MSE as a function of t in Figure 17 for all the samples in our test set. Unlike Examples 1 and 2, in which we could not observe any relationships between the MSE values and Ra values, here we could see that three cases have significantly higher errors than those of the rest. These three cases share the same characteristic in which their Ra_2 values are relatively high, $Ra_2 = 60.26$, $Ra_2 = 74.13$, and $Ra_2 = 74.13$.

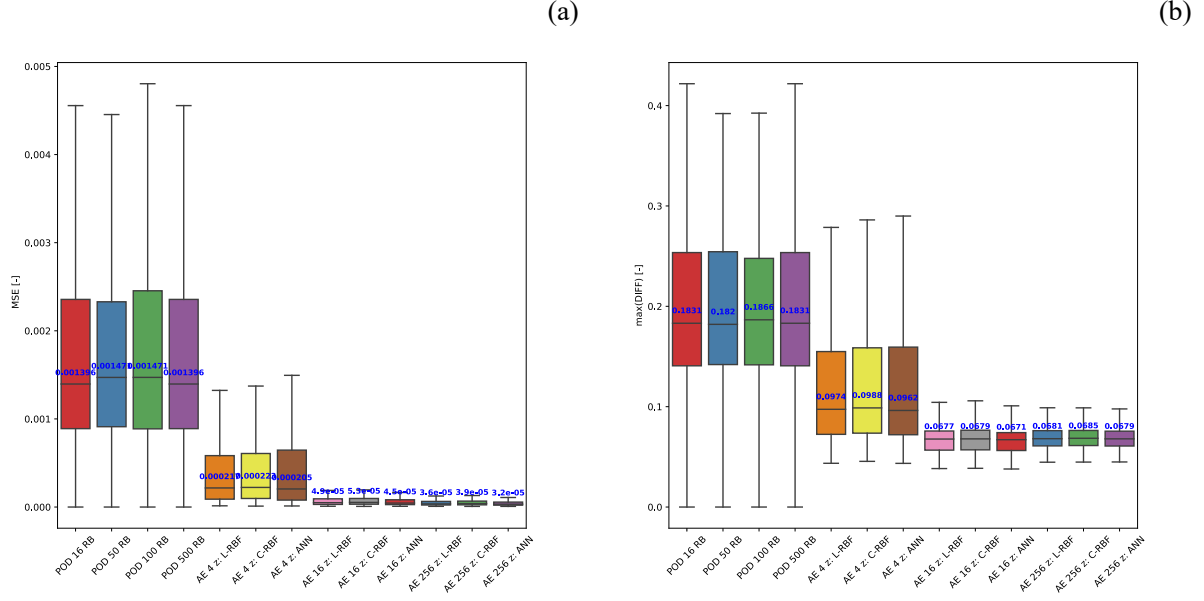


Figure 11: Example 2: Each model's performance on a test set (a) mean square error (MSE) and (b) maximum DIFF (max(DIFF)). Blue text represents a mean value. 16 RB, 50 RB, 100 RB, and 500 RB represent linear compression models with $[N_{\text{int}} = 16, N = 16]$, $[N_{\text{int}} = 50, N = 50]$, $[N_{\text{int}} = 100, N = 100]$, and $[N_{\text{int}} = 500, N = 500]$, respectively. The L-RBF and C-RBF are the nonlinear compression models with RBF with linear function and RBF with cubic function as its approximator, respectively.

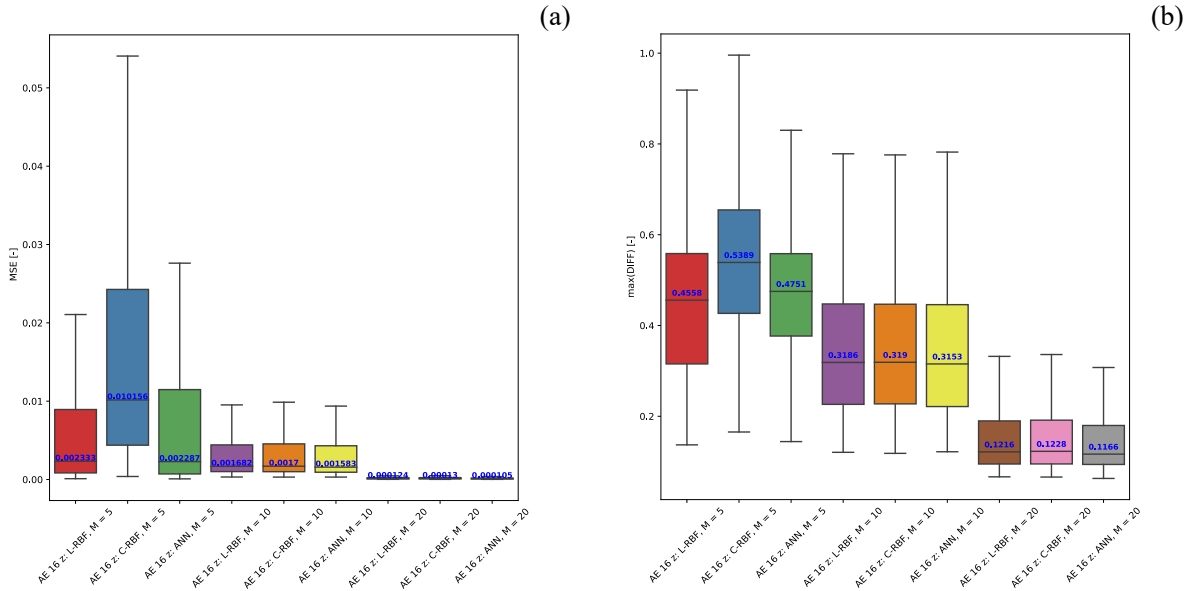


Figure 12: Example 2: Each model's performance on a test set with different number of training data, $M = 5$, $M = 10$, and $M = 20$, (a) mean square error (MSE) and (b) maximum DIFF (max(DIFF)). Blue text represents a mean value. We here only present results of nonlinear approach using $Q = 16$ with L-RBF, C-RBF, or ANN as its approximator.

The reasons that these three cases have considerably higher errors than the rest of the test set stem from how we sample our training and testing sets. We plot our training and testing samples in Figure 18. As the range of Ra_2 spans several orders of magnitude (i.e., $Ra_2 = [0.001, 100.0]$), we sample Ra_2 through its log-scale (i.e., $\log_{10}(Ra_2) = [-3, 2]$) using equispaced distribution for the training set. Consequently, there are not many training samples that lie in a range where Ra_2 values are relatively high (see Figure 18).

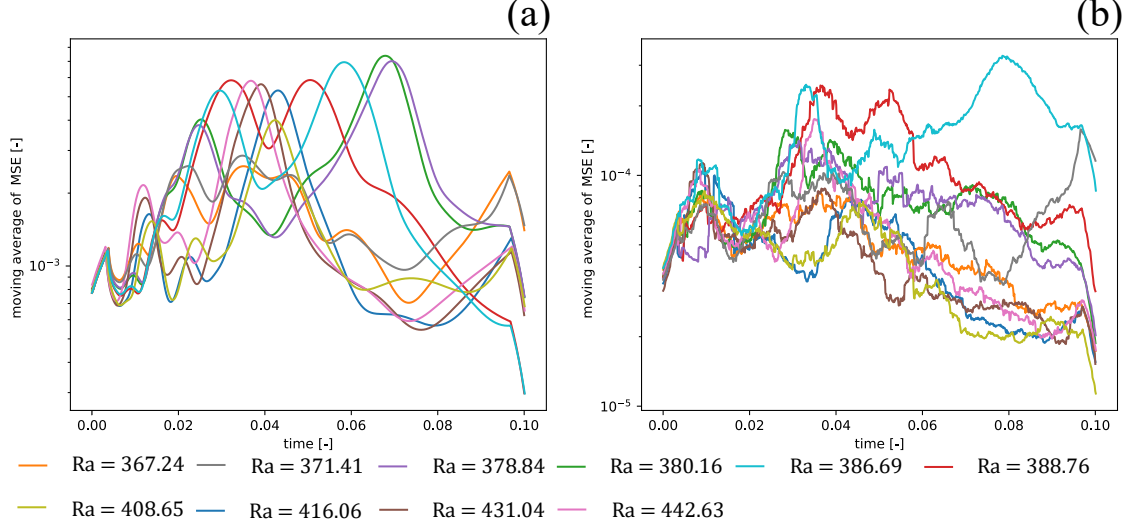


Figure 13: Example 2: 50th moving average of MSE on a test set of (a) POD 16 RB and (b) AE 16 z: ANN.

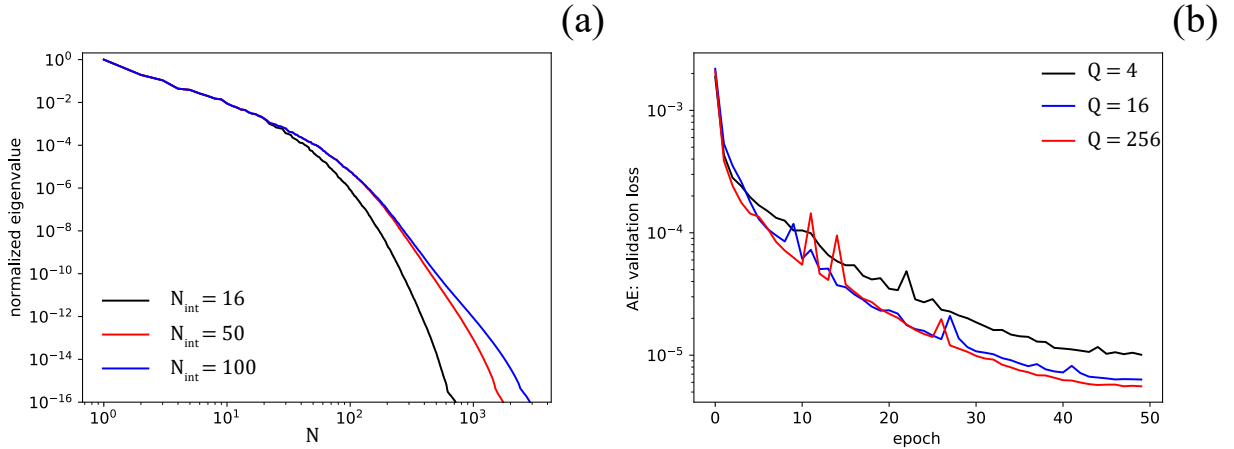


Figure 14: Example 3: (a) normalized eigenvalue as a function of reduced basis and (b) autoencoder validation loss during the training.

The nonlinear compression approach seems to suffer from this sampling technique more than the linear one. To elaborate, for the POD approach, we observe that the MSE values of these three cases are approximately one order of magnitude higher than those of the group. However, MSE values become much higher (about two orders of magnitude) than the rest of the testing cases for the AE models. Therefore, one may want to consider adaptive sampling approaches [Paul-Dubois-Taine and Amsallem, 2015, Vasile et al., 2013, Choi et al., 2020a] when dealing with nonlinear compression models.

5 Discussion

In this section, we will discuss three main aspects of our findings: (1) model accuracy, (2) computational cost, and (3) a suggestion to select between linear and nonlinear non-intrusive reduced order modeling approaches.

5.1 Model accuracy

From the numerical experiments, we observe that the linear and nonlinear approaches can each perform better depending on the problem at hand. The linear approach has a better performance than its nonlinear counterpart, for Example 1.

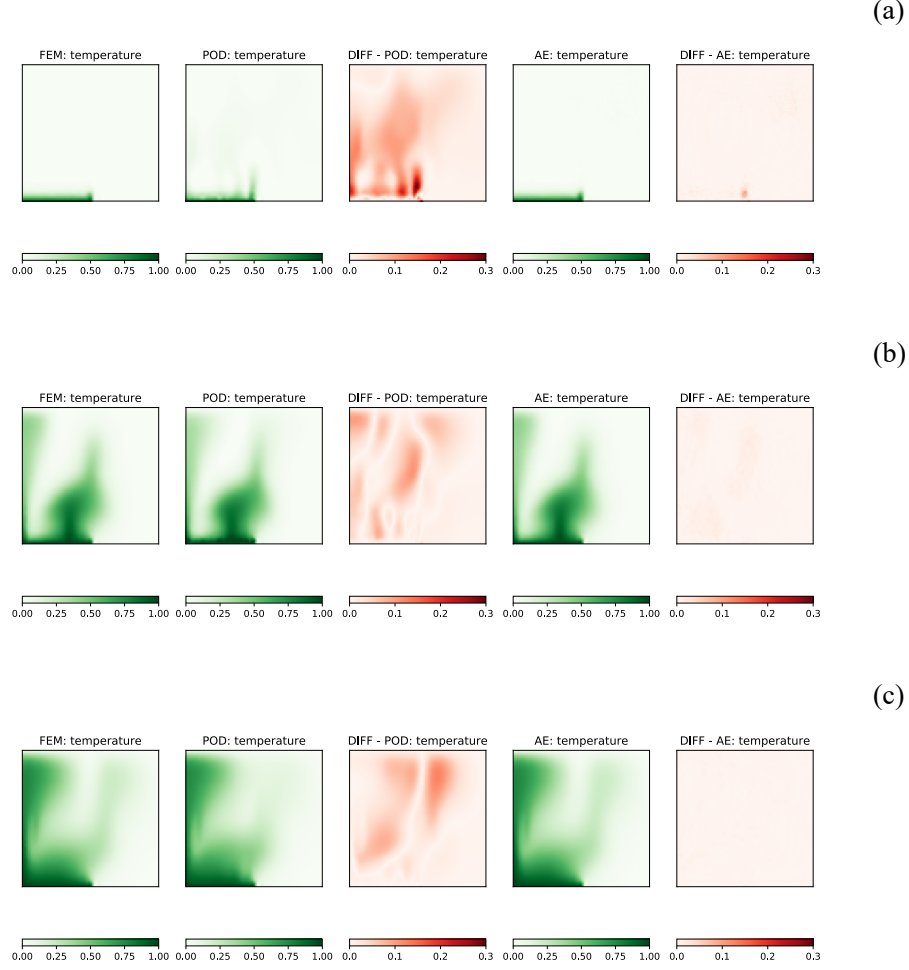


Figure 15: Example 3: test case ($Ra_1 = 357.39$, $Ra_2 = 0.004$) results. (a) $t = 0.001$, (b) $t = 0.03$, and (c) $t = 0.07$. These results are produced by POD 16 RB and AE 16 z: ANN for POD: temperature and AE: temperature, respectively.

The linear compression average of MSE is about one order of magnitude less than that of the nonlinear compression. In Example 2, the AE model with at least 16 latent spaces has MSE of two orders of magnitude less than the POD approach. The same goes for Example 3, where we have more parameters than Examples 1 and 2 (i.e., we have two parameters; Ra_1 and Ra_2).

For all examples, there is no significant accuracy difference among POD models with a different number of reduced bases N (as well as the number of intermediate reduced basis N_{int}). As discussed extensively in Kadeethum et al. [2021b], the errors not only arise in the POD compression process but also during the mapping between the pair (t, μ) and the solution in the reduced linear subspace by ANN. Another observation is, for Examples 2 and 3, as we increase N_{int} , the decay of eigenvalue as a function of N grows slower. This behavior indicates that the model evolution in time requires a large number of N_{int} , which implies that the linear compression approach may not be suitable for Examples 2 and 3. For the nonlinear compression approach, we observe that using three different types of approximators, linear RBF, cubic RBF, and ANN, to map between the pair (t, μ) and the solution in the reduced nonlinear manifold (z) results in approximately the same accuracy. Moreover, the training time and prediction time of each model are not significantly different.

Another interesting observation is that using $M = 40$ the nonlinear approach achieves around five to ten % of maximum relative errors for Examples 1, 2, and 3. On the other hand, the linear approach delivers a wide range of relative errors across Examples 1, 2, and 3. We also test our nonlinear model using different M . As expected, the model's accuracy increases as M increases.

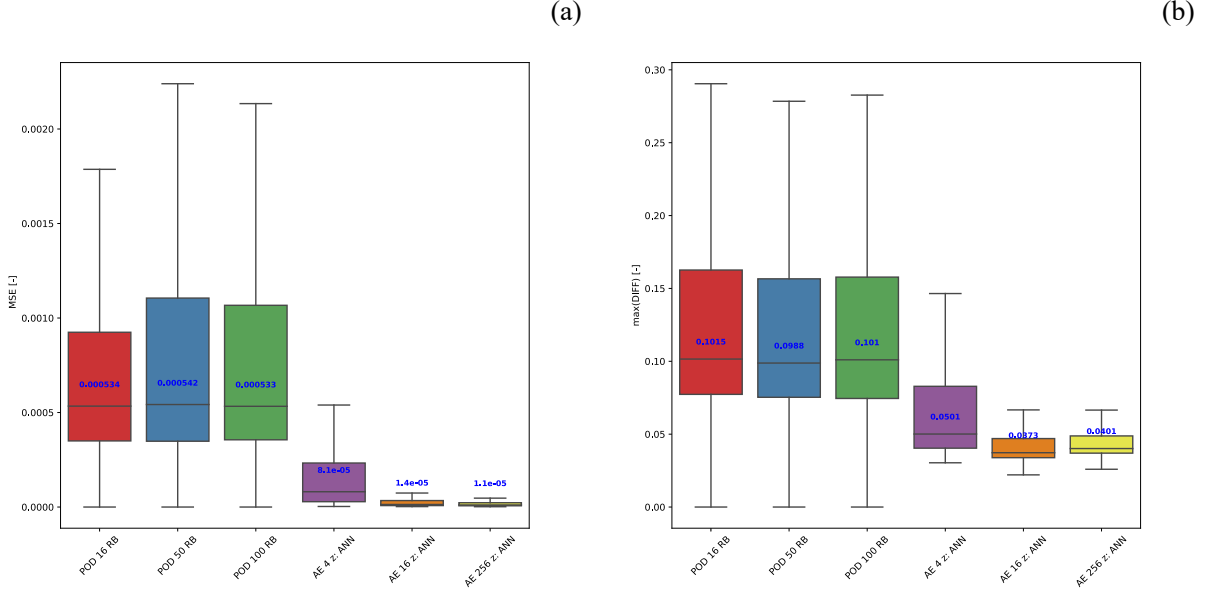


Figure 16: Example 3: Each model's performance on a test set (a) mean square error (MSE) and (b) maximum DIFF (max(DIFF)). Blue text represents a mean value.

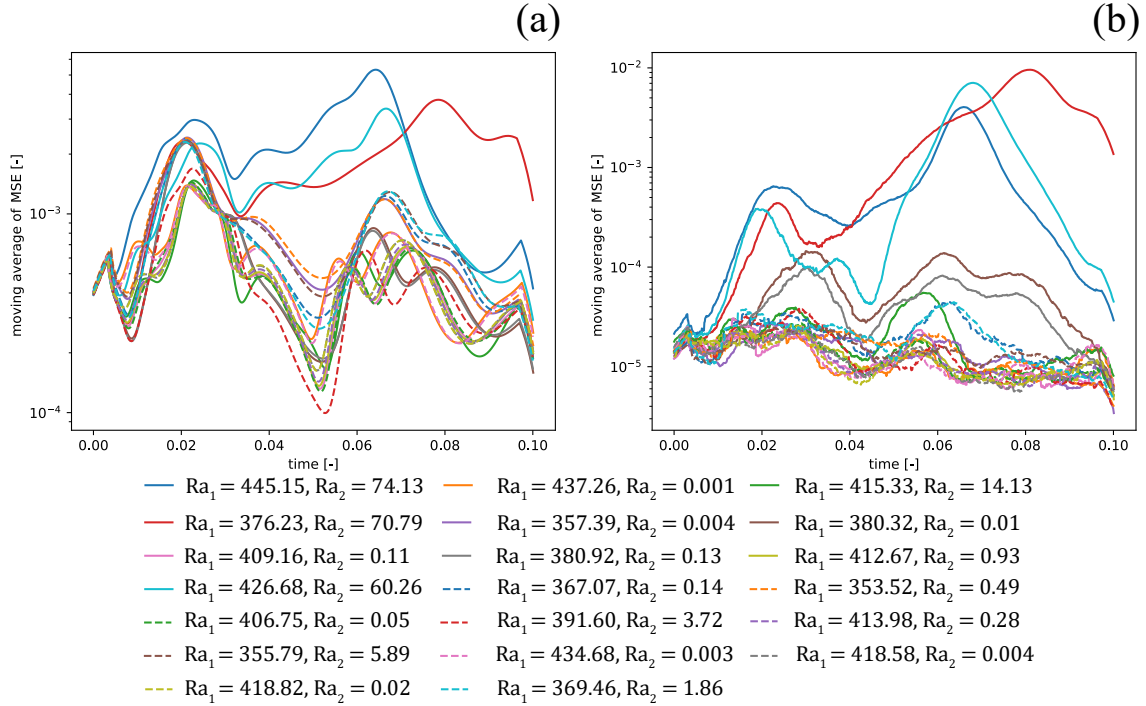


Figure 17: Example 3: 50th moving average of MSE on a test set of (a) POD 16 RB and (b) AE 16 z-ANN. 16 RB, 50 RB, and 100 RB represent linear compression models with $[N_{\text{int}} = 16, N = 16]$, $[N_{\text{int}} = 50, N = 50]$, and $[N_{\text{int}} = 100, N = 100]$, respectively.

In Example 3, we illustrate that the sampling technique used to generate our training set could affect our framework's accuracy. Especially, the performance of the nonlinear approach is substantially influenced by regions of sparse training data (i.e., test cases that lie within the sparse training data zone have MSE values about two orders of magnitude

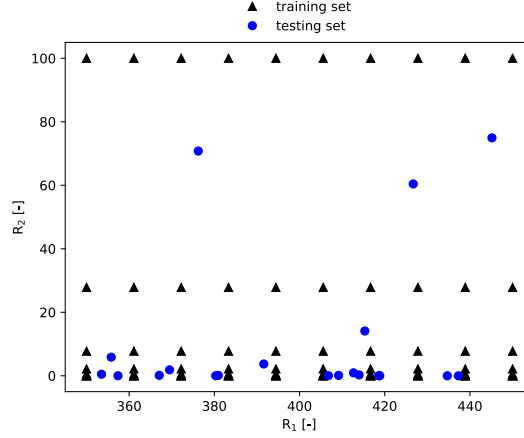


Figure 18: Example 3: training and testing samples: linear scale.

higher than the rest of the testing cases). Hence, we recommend a future study of the application of adaptive sampling approaches [Paul-Dubois-Taine and Amsallem, 2015, Vasile et al., 2013] applied to the nonlinear compression model.

We want to emphasize that the linear approach could handle data from unstructured mesh, which is beneficial because it is applicable to complex geometries. Our nonlinear approach; however, relies on convolutional layers (without convolutional layers, its accuracy decreased as shown in Appendix E); hence, to apply this model to more complex geometries, one may require additional techniques such as graph convolutional networks [Kipf and Welling, 2016] or space-filling curves [Heaney et al., 2020].

5.2 Computational cost

We perform FOM, POD, L_2 projection, RBF, and linear reconstruction on AMD Ryzen Threadripper 3970X. The training of AE and ANN and nonlinear reconstruction are done by a single Quadro RTX 6000. We note that without using Quadro RTX 6000, our AE model requires impractical training time on AMD Ryzen Threadripper 3970X. The FOM is done using multiphenics (<https://github.com/multiphenics/multiphenics>) and FEniCS (<https://fenicsproject.org/>) frameworks. The POD is done using RBniCS (<https://github.com/RBniCS/RBniCS/>). The ANN and AE models are developed based on PyTorch (<https://pytorch.org/>), and the RBF is performed using SciPy (<https://www.scipy.org/>).

The computational time used to develop our ROM can be broken down into three main parts: (i) generation of training data through FOM - the second step in Figure 1, (ii) data compression - the third step in Figure 1, and (iii) mapping of t and μ to reduced subspace - the fourth step in Figure 1. We note that initialization of μ - the first step in Figure 1 and prediction or online phase - the fifth step in Figure 1 are relatively much cheaper and insignificant compared to steps 2, 3, and 4.

The generation of training data through FOM - the second step in Figure 1, requires the highest computational resources. On average, each FOM snapshot, each $\mu^{(i)}$ for all t , takes about two hours on AMD Ryzen Threadripper 3970X (4 threads). Again, we note that our FOM utilizes the adaptive time-stepping, see Equation (A.4); hence, each $\mu^{(i)}$ may require a substantially different computational time. To elaborate, cases that have higher Ra usually have a smaller time-step (N^t becomes larger); and subsequently, they require more time to complete.

For the data compression step - the third step in Figure 1, the linear compression technique usually takes a longer time than its nonlinear counterpart. However, we note that this may not be a fair comparison as we perform POD and AE using different platforms and machines. Moreover, we want to emphasize that without using *nested* POD technique, our linear compression approach would not be able to complete its operation in a timely manner. On average, the POD operation takes about five to eight hours, while the AE model takes approximately four to six hours. We note that this comparison is made using different machines. As mentioned previously, the POD is computed using CPU while the AE is trained using GPU. We want to emphasize that training our AE model using CPU would require an impractical training time. Moreover, using incremental SVD or randomized SVD may reduce our computational time of POD significantly [Choi et al., 2019b].

The mapping of t and μ to reduced subspace - the fourth step in Figure 1 is the cheapest among the three main parts. For linear compression, we only use the ANN model as a mapping tool between t and μ and linear subspace w . The training of the ANN model used throughout this study takes about one and a half to two hours. For nonlinear compression, as mentioned previously, using linear RBF, cubic RBF, and ANN, to map the time/parameters pair (t and μ) to the approximation of the snapshot in the nonlinear manifolds (z) leads to approximately the same accuracy. The linear RBF is slightly cheaper than the cubic RBF and ANN. Again, we note that this may not be a fair comparison because even though we use the same machine for these calculations, we build our RBF models on SciPy but the ANN model on PyTorch. These three processes, on average, take about one to two and a half hours depending on the value of Q .

The computational time used during the prediction or the online phase - the fifth step in Figure 1 -, for both linear and nonlinear approaches, is a completely different story. Once the ROM is trained, it could be used in an extremely fast fashion. One inquiry - a pair of t^k and $\mu^{(i)}$ takes only several milliseconds. Hence, one typically enjoys an inexpensive online phase compared to FOM for each inquiry. To elaborate, one FOM simulation, i.e., $\mu^{(i)}$ for all t , takes two hours, as mentioned previously, but one ROM simulation would take approximately one second given that you require an evaluation of your quantities of interest at all timestamps used in FOM, $0 =: t^0 < t^1 < \dots < t^N := \tau$. In practice, however, the ROM is not bound by CFL condition; hence, it can deliver the quantities of interest at any specific timestamps without going through any timestamps in between in order to satisfy CFL condition. Assuming we only require our quantities of interest at the final time, for Example 2, our ROM could provide a speed-up of 7×10^6 . In the worst-case scenario where an evaluation of your quantities of interest at all timestamps used in FOM is required, our framework could still provide a speed-up of 7×10^3 . In short, our framework could provide speed-up of 7×10^3 to 7×10^6 .

5.3 Linear vs. nonlinear approach?

As discussed in previous sections, the linear approach performs better in Example 1, while the proposed nonlinear approach delivers superior performance in Examples 2 and 3. A popular indicator to determine if the linear approach will work well or not is to see the singular value decay (or the eigenvalue decay). If the eigenvalue decays fast, which is the case for Example 1 (see the bottom row and first column of Figure 19), then the linear approach will work well. Alternatively, we here propose a figurative way to estimate which method will perform better without performing an actual compression and reconstruction. We visualize the linear and nonlinear manifolds of each example using principal component analysis (PCA) [Abdi and Williams, 2010] and t-Distributed Stochastic Neighbor Embedding (t-SNE) [Van der Maaten and Hinton, 2008] in Figure 19. We note that this visualization is done directly on the data produced from FOM, T_h in this case; hence, this can be done before the construction of ROM. To be precise, this visualization could be done between steps 2 and 3 presented in Figure 1. These plots are done using SciPy (<https://www.scipy.org/>) and created using data from our test set, and each color represents a specific $\mu^{(i)}$.

The PCA could be considered a linear subspace visualization, while the t-SNE is a nonlinear visualization manifold. From Figure 19, we observe that the PCA and t-SNE plots are not much different, for Example 1. However, the PCA and t-SNE plots are substantially different for Examples 2 and 3. This behavior may imply that Example 1 is less complex, and its reduced representation could be fitted into linear subspace. Examples 2 and 3, on the other hand, exhibit more complex behavior, which leads to substantially different behavior between linear and nonlinear approaches. Hence, a qualitative comparison between PCA and t-SNE plots may indicate the performance of linear and nonlinear non-intrusive ROM approaches. We note that this observation requires further investigation before more definitive conclusions can be reached.

6 Conclusion

We present a non-intrusive reduced order model of natural convection in porous media. Our reduced order model is developed based on deep convolutional autoencoder as data compression and reconstruction tools and a regressor, radial basis function regression, or artificial neural networks for mapping our parameter space to nonlinear manifolds. The framework could handle data from a finite element model with adaptive time-stepping, commonly in the natural convection problem since Courant–Friedrichs–Lewy (CFL) condition controls the time-step size. During an online phase, our framework is not bound by CFL condition; hence, it could deliver quantities of interest at any given time without going through timestamps in between. Therefore, our reduced order model is much faster than the finite element model (speed-up of up to 7×10^6), while its accuracy, in the worst-case scenario, still lies within a mean squared error of 0.07. We also provide comprehensive comparisons between the linear and nonlinear compression approaches. We illustrate that in specific settings, the nonlinear compression outperforms its linear counterpart and vice versa. We suggest that it might be possible to use a quantitative comparison of subspace visualization using principal component analysis (PCA) and t-Distributed Stochastic Neighbor Embedding (t-SNE) to indicate which method will perform better.

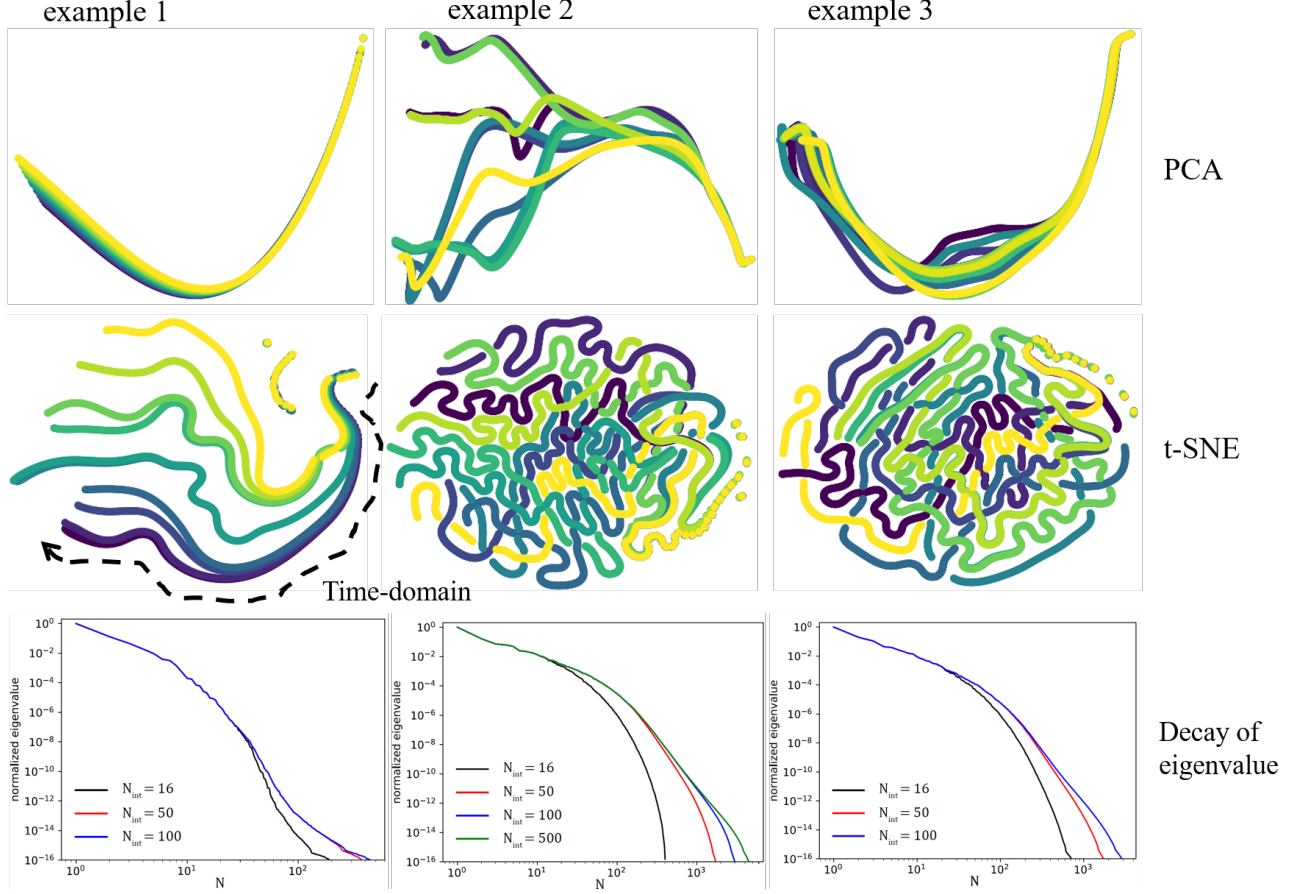


Figure 19: Subspace of T_h visualization using principal component analysis (PCA) and t-Distributed Stochastic Neighbor Embedding (t-SNE). Each color represents each $\mu^{(i)}$. The bottom row shows a decay of eigenvalue as a function of a number of reduced linear basis (N). These plots are created using data from our test set.

7 Acknowledgments

FB thanks Horizon 2020 Program for Grant H2020 ERC CoG 2015 AROMA-CFD project 681447 (PI Prof. Gianluigi Rozza) that supported the development of RBniCS and multiphenics, and the project “Numerical modeling of flows in porous media” organized at the Catholic University of the Sacred Heart. YC acknowledges LDRD funds (21-FS-042) from Lawrence Livermore National Laboratory (LLNL-JRNL-824706). Lawrence Livermore National Laboratory is operated by Lawrence Livermore National Security, LLC, for the U.S. Department of Energy, National Nuclear Security Administration under Contract DE-AC52-07NA27344. DO acknowledges support from Los Alamos National Laboratory’s Laboratory Directed Research and Development Early Career Award (20200575ECR). HY was supported by the Laboratory Directed Research and Development program at Sandia National Laboratories. Sandia National Laboratories is a multimission laboratory managed and operated by National Technology and Engineering Solutions of Sandia LLC, a wholly owned subsidiary of Honeywell International Inc. for the U.S. Department of Energy’s National Nuclear Security Administration under contract DE-NA0003525. NB acknowledges startup support from the Sibley School of Mechanical and Aerospace Engineering, Cornell University.

Appendix A Finite element discretization and solution

In this section, we describe the numerical methods for solving the governing system described in Section 2. Here, we utilize a combination of a mixed finite element method for spatial discretization, and employ a backward differentiation formula for temporal discretization.

A.1 Domain discretization and geometrical operators

We follow the framework proposed in Kadeethum et al. [2021a]. We here briefly introduce the notations used throughout this section. Let \mathcal{T}_h be a shape-regular triangulation obtained by a partition of Ω into d -simplices (triangles in $d = 2$, for example). For each cell $\mathcal{T} \in \mathcal{T}_h$, we denote by $h_{\mathcal{T}}$ the diameter of \mathcal{T} , and we set $h_{\max} = \max_{\mathcal{T} \in \mathcal{T}_h} h_{\mathcal{T}}$ and $h_{\min} = \min_{\mathcal{T} \in \mathcal{T}_h} h_{\mathcal{T}}$. We further denote by \mathcal{E}_h the set of all faces (i.e., $d - 1$ dimensional entities connected to at least a $T \in \mathcal{T}_h$) and by \mathcal{E}_h^I and \mathcal{E}_h^{∂} the collection of all interior and boundary facets, respectively. The boundary set \mathcal{E}_h^{∂} is decomposed as $\mathcal{E}_h^{D,m} \cup \mathcal{E}_h^{N,m}$, where $\mathcal{E}_h^{D,m}$ and $\mathcal{E}_h^{N,m}$ are two disjoint subsets associated with the Dirichlet boundary faces on $\partial\Omega_p$ and the Neumann boundary faces on $\partial\Omega_q$ as defined in Equation (7). For Equation (9), \mathcal{E}_h^{∂} is decomposed as $\mathcal{E}_h^{D,T} \cup \mathcal{E}_h^{\text{In}} \cup \mathcal{E}_h^{\text{Out}}$ defined based on $\partial\Omega_T$, $\partial\Omega_{\text{In}}$, $\partial\Omega_{\text{Out}}$, respectively.

Next,

$$e = \partial\mathcal{T}^+ \cap \partial\mathcal{T}^-, \quad e \in \mathcal{E}_h^I,$$

where \mathcal{T}^+ and \mathcal{T}^- are the two neighboring elements to e . We denote by h_e the characteristic length of e calculated as

$$h_e := \frac{\text{meas}(\mathcal{T}^+) + \text{meas}(\mathcal{T}^-)}{2 \text{meas}(e)}, \quad (\text{A.1})$$

depending on the argument, $\text{meas}(\cdot)$ represents the measure of a cell ($d = 3$) or of a facet ($d = 2$).

Let \mathbf{n}^+ and \mathbf{n}^- be the outward unit normal vectors to $\partial\mathcal{T}^+$ and $\partial\mathcal{T}^-$, respectively. For any given scalar function $\zeta : \mathcal{T}_h \rightarrow \mathbb{R}$ and vector function $\boldsymbol{\sigma} : \mathcal{T}_h \rightarrow \mathbb{R}^d$, we denote by ζ^{\pm} and $\boldsymbol{\sigma}^{\pm}$ the restrictions of ζ and $\boldsymbol{\sigma}$ to \mathcal{T}^{\pm} , respectively. Subsequently, we define the weighted average operator as

$$\{\zeta\}_{\delta e} = \delta_e \zeta^+ + (1 - \delta_e) \zeta^-, \quad \text{on } e \in \mathcal{E}_h^I, \quad (\text{A.2})$$

and

$$\{\boldsymbol{\sigma}\}_{\delta e} = \delta_e \boldsymbol{\sigma}^+ + (1 - \delta_e) \boldsymbol{\sigma}^-, \quad \text{on } e \in \mathcal{E}_h^I, \quad (\text{A.3})$$

where δ_e is weighted average, which is 0.5 throughout this manuscript. The jump across an interior edge will be defined as

$$[\![\zeta]\!] = \zeta^+ \mathbf{n}^+ + \zeta^- \mathbf{n}^- \quad \text{and} \quad [\![\boldsymbol{\sigma}]\!] = \boldsymbol{\sigma}^+ \cdot \mathbf{n}^+ + \boldsymbol{\sigma}^- \cdot \mathbf{n}^- \quad \text{on } e \in \mathcal{E}_h^I.$$

Finally, for $e \in \mathcal{E}_h^{\partial}$, we set $\{\zeta\}_{\delta_e} := \zeta$ and $\{\boldsymbol{\sigma}\}_{\delta_e} := \boldsymbol{\sigma}$ for what concerns the definition of the weighted average operator, and $[\![\zeta]\!] := \zeta \mathbf{n}$ and $[\![\boldsymbol{\sigma}]\!] := \boldsymbol{\sigma} \cdot \mathbf{n}$ as definition of the jump operator.

A.2 Temporal discretization

The time domain $\mathbb{T} = (0, \tau]$ is partitioned into N^t subintervals such that $0 =: t^0 < t^1 < \dots < t^N := \tau$. The length of each subinterval Δt^{n-1} is defined as $\Delta t^{n-1} = t^n - t^{n-1}$ where n represents the current time-step and $n - 1$ is previous time-step. We assume that the user provides the initial Δt^0 , while an adaptive procedure is carried out to choose Δt^{n-1} , $n > 1$, as follows

$$\Delta t^{n-1} := \begin{cases} \text{CFL} \frac{h_l}{\|\mathbf{u}^{n-1}\|_{\infty}} & \text{if } \Delta t^{n-1} \leq \Delta t_{\max} \\ \Delta t_{\max} & \text{if } \Delta t^{n-1} > \Delta t_{\max}, \end{cases} \quad (\text{A.4})$$

where CFL is a constant that the user can provide according to the Courant-Friedrichs-Lewy condition [Courant et al., 1967], $\|\cdot\|_{\infty}$ is the maximum norm of a vector function, and Δt_{\max} is a maximum allowed time-step. Note that we use Δt_{\max} to control Δt^n when the model approaches a steady-state condition since $\|\mathbf{u}^{n-1}\|_{\infty}$ may approach zero, which would lead to a very large ratio $\frac{h_l}{\|\mathbf{u}^{n-1}\|_{\infty}}$.

Let $\varphi(\cdot, t)$ be a scalar function and φ^n be its approximation at time t^n , i.e. $\varphi^n \approx \varphi(t^n)$. We employ the following backward differentiation formula [Ibrahim et al., 2007, Akinfenwa et al., 2013, Lee et al., 2018]

$$\text{BDF}_m(\varphi^n) := \begin{cases} \frac{1}{\Delta t^n} (\varphi^n - \varphi^{n-1}) & m = 1 \\ \frac{2}{3\Delta t^n} (3\varphi^n - 4\varphi^{n-1} + \varphi^{n-2}) & m = 2 \\ \frac{6}{5\Delta t^n} (11\varphi^n - 18\varphi^{n-1} + 9\varphi^{n-2} - 2\varphi^{n-3}) & m = 3 \\ \frac{12}{13\Delta t^n} (25\varphi^n - 48\varphi^{n-1} + 36\varphi^{n-2} - 16\varphi^{n-3} + 3\varphi^{n-4}) & m = 4 \end{cases} \quad (\text{A.5})$$

for the discretization of the time derivative of $\varphi(\cdot, t)$ at time t^n .

A.3 Spatial discretization

Following Kadeethum et al. [2021a], the fluid velocity and pressure fields in Equation (7) are discretized by the Brezzi-Douglas-Marini (BDM) element [Brezzi and Fortin, 2012] and the piecewise constants element, respectively, to ensure local mass conservation. The temperature field in Equation (9) is discretized by the enriched Galerkin (EG) method [Lee et al., 2016, Sun and Liu, 2009].

We begin with defining the BDM function space as follows [Brezzi and Fortin, 2012]

$$\mathcal{U}_h^{\text{BDM}_k}(\mathcal{T}_h) := \{\psi_u \in H(\text{div}, \Omega) : \psi_u|_{\mathcal{T}} \in \text{BDM}(\mathcal{T}), \forall \mathcal{T} \in \mathcal{T}_h\}. \quad (\text{A.6})$$

Here, ψ_u denotes a generic function of $\mathcal{U}_h^{\text{BDM}_k}(\mathcal{T}_h)$ and $\text{BDM}(\mathcal{T})$ is defined according to [Brezzi and Fortin, 2012]. Next, the discontinuous Galerkin (DG) function space is

$$\mathcal{P}_h^{\text{DG}_k}(\mathcal{T}_h) := \{\psi_p \in L^2(\Omega) : \psi_p|_{\mathcal{T}} \in \mathbb{P}_k(\mathcal{T}), \forall \mathcal{T} \in \mathcal{T}_h\}, \quad (\text{A.7})$$

where $L^2(\Omega)$ is the space of square-integrable scalar functions, and ψ_p a generic function of $\mathcal{P}_h^{\text{DG}_k}(\mathcal{T}_h)$. We note that $\mathcal{P}_h^{\text{DG}_0}(\mathcal{T}_h)$ represents the piecewise constants function. We then define the finite element space for the continuous Galerkin (CG) function space for a scalar-valued function

$$\mathcal{P}_h^{\text{CG}_k}(\mathcal{T}_h) := \{\psi_T \in \mathbb{C}^0(\Omega) : \psi_T|_{\mathcal{T}} \in \mathbb{P}_k(\mathcal{T}), \forall \mathcal{T} \in \mathcal{T}_h\}. \quad (\text{A.8})$$

Here, $\mathbb{C}^0(\Omega) := \mathbb{C}^0(\Omega; \mathbb{R})$ denotes the space of scalar-valued piecewise continuous polynomials, and $\mathbb{P}_k(\mathcal{T}) := \mathbb{P}_k(\mathcal{T}; \mathbb{R})$ is the space of polynomials of degree at most k over each element \mathcal{T} . Finally, the EG finite element space with polynomial order k is

$$\mathcal{P}_h^{\text{EG}_k}(\mathcal{T}_h) := \mathcal{P}_h^{\text{CG}_k}(\mathcal{T}_h) \oplus \mathcal{P}_h^{\text{DG}_0}(\mathcal{T}_h), \quad (\text{A.9})$$

where ψ_T denotes a generic function of $\mathcal{P}_h^{\text{EG}_k}(\mathcal{T}_h)$ (as well as $\mathcal{P}_h^{\text{CG}_k}(\mathcal{T}_h)$).

A.4 Full discretization

We now present the fully discrete form of Equations (7) and (9) using the above-described combination of finite element spaces. In particular, we seek the approximated velocity $\mathbf{u}_h \in \mathcal{U}_h^{\text{BDM}_1}(\mathcal{T}_h)$, approximated fluid pressure $p_h \in \mathcal{P}_h^{\text{DG}_0}(\mathcal{T}_h)$, and approximated $T_h \in \mathcal{P}_h^{\text{EG}_1}(\mathcal{T}_h)$. The weak form of the first part of mass balance Equation (7) is obtained multiplying by $\psi_u \in \mathcal{U}_h^{\text{BDM}_1}(\mathcal{T}_h)$ and integrating by parts, resulting in

$$\mathcal{N}_u(\psi_u; \mathbf{u}_h^n, p_h^n, T_h^n) = 0, \quad \forall \psi_u \in \mathcal{U}_h^{\text{BDM}_1}(\mathcal{T}_h), \quad (\text{A.10})$$

for each time-step t^n , where

$$\begin{aligned} \mathcal{N}_u(\psi_u; \mathbf{u}_h^n, p_h^n, T_h^n) &= \sum_{\mathcal{T} \in \mathcal{T}_h} \int_{\mathcal{T}} \mathbf{u}_h^n \cdot \psi_u \, dV + \sum_{\mathcal{T} \in \mathcal{T}_h} \int_{\mathcal{T}} p_h^n \nabla \cdot \psi_u \, dV - \sum_{\mathcal{T} \in \mathcal{T}_h} \int_{\mathcal{T}} \mathbf{z} \text{Ra} T_h^n \cdot \psi_u \, dV \\ &+ \sum_{e \in \mathcal{E}_h^{D,m}} \int_e p_D \psi_u \cdot \mathbf{n} \, dS, \quad \forall \psi_u \in \mathcal{U}_h^{\text{BDM}_1}(\mathcal{T}_h). \end{aligned}$$

Here, $\int_{\mathcal{T}} \cdot dV$ and $\int_e \cdot dS$ refer to volume and surface integrals, respectively. Furthermore, the notation for $\mathcal{N}_u(\psi_u; \mathbf{u}_h^n, p_h^n, T_h^n)$ in Equation (A.10) highlights before the semicolon the test function, and after the semicolon the nonlinear dependence on discrete solutions to the coupled problem. The same notation will be used hereafter for the remaining equations.

Then we multiply the $\nabla \cdot \mathbf{u} = 0$ of Equation (7) by $\psi_p \in \mathcal{P}_h^{\text{DG}_0}(\mathcal{T}_h)$ and integrating by parts as follows

$$\mathcal{N}_p(\psi_p; \mathbf{u}_h^n, p_h^n, T_h^n) = 0, \quad \forall \psi_p \in \mathcal{P}_h^{\text{DG}_0}(\mathcal{T}_h), \quad (\text{A.11})$$

for each time-step t^n , where

$$\mathcal{N}_p(\psi_p; \mathbf{u}_h^n, p_h^n, T_h^n) = \sum_{\mathcal{T} \in \mathcal{T}_h} \int_{\mathcal{T}} \nabla \cdot \mathbf{u}_h^n \psi_p dV, \quad \forall \psi_p \in \mathcal{P}_h^{\text{DG}_0}(\mathcal{T}_h).$$

Next, we discretize Equation (9)

$$\mathcal{N}_T(\psi_T; \mathbf{u}_h^n, p_h^n, T_h^n) = 0, \quad \forall \psi_T \in \mathcal{P}_h^{\text{EG}_1}(\mathcal{T}_h) \quad (\text{A.12})$$

for each time-step t^n , where

$$\begin{aligned} \mathcal{N}_T(\psi_T; \mathbf{u}_h^n, p_h^n, T_h^n) = & \sum_{\mathcal{T} \in \mathcal{T}_h} \int_{\mathcal{T}} \text{BDF}_4(T_h^n) \psi_T dV + \sum_{\mathcal{T} \in \mathcal{T}_h} \int_{\mathcal{T}} \nabla T_h^n \cdot \nabla \psi_T dV \\ & - \sum_{e \in \mathcal{E}_h^I \cup \mathcal{E}_h^{D,T}} \int_e \{\nabla T_h^n\}_{\delta_e} \cdot \llbracket \psi_T \rrbracket dS + \theta \sum_{e \in \mathcal{E}_h^I \cup \mathcal{E}_h^{D,T}} \int_e \{\nabla \psi_T\}_{\delta_e} \cdot \llbracket T_h^n \rrbracket dS \\ & + \sum_{e \in \mathcal{E}_h^I \cup \mathcal{E}_h^{D,T}} \int_e \frac{\beta}{h_e} \llbracket T_h^n \rrbracket \cdot \llbracket \psi_T \rrbracket dS - \sum_{\mathcal{T} \in \mathcal{T}_h} \int_{\mathcal{T}} \mathbf{u}_h^n T_h^n \cdot \nabla \psi_T dV \\ & + \sum_{e \in \mathcal{E}_h^I} \int_e \mathbf{u}_h^n \cdot \mathbf{n} T_h^{\text{up}} \llbracket \psi_T \rrbracket dS + \sum_{e \in \mathcal{E}_h^{D,T}} \int_e \nabla \psi_T \cdot T_D \mathbf{n} dS - \sum_{e \in \mathcal{E}_h^{D,T}} \int_e \frac{\beta}{h_e} \llbracket \psi_T \rrbracket \cdot T_D \mathbf{n} dS \\ & + \sum_{e \in \mathcal{E}_h^{\text{out}}} \int_e \mathbf{u}_h^n \cdot \mathbf{n} T_h^n \psi_T dS + \sum_{e \in \mathcal{E}_h^{\text{in}}} \int_e \mathbf{u}_h^n \cdot \mathbf{n} T_{\text{in}} \psi_T dS - \sum_{T \in \mathcal{T}_h} \int_T f_c \psi_T dV, \quad \forall \psi_T \in \mathcal{P}_h^{\text{EG}_1}(\mathcal{T}_h). \end{aligned}$$

Two parameters θ and β define corresponding interior penalty methods. The discretization becomes the symmetric interior penalty Galerkin method (SIPG) when $\theta = -1$, the incomplete interior penalty Galerkin method (IIPG) when $\theta = 0$, and the non-symmetric interior penalty Galerkin method (NIPG) when $\theta = 1$ [Riviere, 2008]. In this study, we set $\theta = 0$ and $\beta = 1.1$ throughout this paper [Kadeethum et al., 2021a]. Also, T_h^{up} is an upwind value of T_h^n defined as [Riviere and Wheeler, 2000, Riviere, 2008]:

$$T_h^{\text{up}} = \begin{cases} T_h^{n+} & \text{if } \mathbf{u}_h^n \cdot \mathbf{n} \geq 0 \\ T_h^{n-} & \text{if } \mathbf{u}_h^n \cdot \mathbf{n} < 0 \end{cases} \quad \forall e = \partial \mathcal{T}^+ \cap \partial \mathcal{T}^- \quad (\text{A.13})$$

where T_h^{n+} and T_h^{n-} correspond to T_h^n of \mathcal{T}^+ and \mathcal{T}^- , respectively.

Appendix B Information on nested proper orthogonal decomposition (POD)

Let $\mu^{(i)}$ be a parameter instance in the training set, $i = 1, \dots, M$. The corresponding T_h snapshot associated to $\mu^{(i)}$ contains

$$\mathbb{S}_T^{(i)} = \left[T_h(\cdot; t^0, \mu^{(i)}), \dots, T_h(\cdot; t^{N^t}, \mu^{(i)}) \right] \in \mathbb{R}^{N_h^T \times N^t}. \quad (\text{B.14})$$

where $T_h(\cdot; t^n, \mu^{(i)})$ represent the temperature field at time t^n and parameter instance $\mu^{(i)}$. We recall that N_h^T is the number of DOFs in the temperature finite element space, and N^t is the total number of time-steps corresponding

to specific μ . In this study, N_h^T is constant (i.e., the mesh and finite element function space remain the same), but N^t varies because our finite element solver utilizes an adaptive time-stepping (see Equation (A.4)). Therefore, each snapshot has a different N^t even though each snapshot utilizes the same initial and final time (i.e., the same starting and endpoints but a different number of intervals).

The nested POD algorithm can be summarized in the two following sequential stages:

- 1) *compression on the temporal evolution*: for each parameter instance $\mu^{(i)}$ in the training set compress the temporal evolution stored in $\mathbb{S}_T^{(i)} \in \mathbb{R}^{N_h^T \times N^t}$ by means of a POD, retaining only the first $N_{\text{int}} \ll N^t$ modes. A compressed matrix $\tilde{\mathbb{S}}_T^{(i)} \in \mathbb{R}^{N_h^T \times N_{\text{int}}}$ is then assembled by storing by column the first N_{int} modes, scaled by the respective singular values. The value of N_{int} can be chosen according to energy criteria (and thus it will be, in general, depending on the index i) or can be fixed a priori (as we do in this study), and is typically considerably smaller than the number of time-steps N^t .
- 2) *compression on the parameter space*: after the temporal evolution of each parameter instance has been compressed, one can assemble the following matrix

$$\tilde{\mathbb{S}}_T = [\tilde{\mathbb{S}}_T^{(1)}, \dots, \tilde{\mathbb{S}}_T^{(M)}] \in \mathbb{R}^{N_h^T \times N_{\text{int}} M}. \quad (\text{B.15})$$

by horizontally stacking all matrices $\tilde{\mathbb{S}}_T^{(i)}$, $i = 1, \dots, M$. We then perform the singular value decomposition (SVD) of $\tilde{\mathbb{S}}_T$ as

$$\tilde{\mathbb{S}}_T = \mathbb{W} \begin{bmatrix} \mathbb{D} & 0 \\ 0 & 0 \end{bmatrix} \mathbb{B}^\top \quad (\text{B.16})$$

where $\mathbb{W} = [\mathbf{w}_1, \dots, \mathbf{w}_{N_h^T}] \in \mathbb{R}^{N_h^T \times N_h^T}$ and $\mathbb{B} = [\mathbf{b}_1, \dots, \mathbf{b}_{N_{\text{int}} M}] \in \mathbb{R}^{N_{\text{int}} M \times N_{\text{int}} M}$ are orthogonal matrices, $\mathbb{D} = \text{diag}(d_1, \dots, d_r) \in \mathbb{R}^{r \times r}$ is a diagonal matrix, with singular values $d_1 \geq d_2 \geq \dots \geq d_r > 0$. Here, r is the number of non-zero singular values and $r \leq \min\{N_h^T, N_{\text{int}} M\}$. The columns of \mathbb{W} are called left singular vectors of $\tilde{\mathbb{S}}_T$, and the columns of \mathbb{B} are called right singular vectors of $\tilde{\mathbb{S}}_T$. To carry out a dimensionality reduction, the POD basis of rank $N \ll r$ consists of the first N left singular vectors of $\tilde{\mathbb{S}}_T$, and it has the property of minimizing the projection error defined by

$$\{\mathbf{w}_1, \dots, \mathbf{w}_N\} = \arg \min \left\{ \varepsilon(\tilde{\mathbf{w}}_1, \dots, \tilde{\mathbf{w}}_N) = \sum_{i=1}^M \sum_{k=0}^{N_{\text{int}}} \left\| T_h(\cdot; t^k, \mu^{(i)}) - \sum_{n=1}^N \left(T_h(\cdot; t^k, \mu^{(i)}), \tilde{\mathbf{w}}_n \right)_T \tilde{\mathbf{w}}_n \right\|_T^2 \right\} \quad (\text{B.17})$$

among all the orthonormal bases $\{\tilde{\mathbf{w}}_1, \dots, \tilde{\mathbf{w}}_N\} \subset \mathbb{R}^{N_h^T}$. Here $(\cdot, \cdot)_T$ denotes an inner product for the temperature space, while $\|\cdot\|_T$ its induced norm. The reduced basis space \mathcal{T}_N is then defined as the span of $\{\mathbf{w}_1, \dots, \mathbf{w}_N\}$.

Appendix C Information on the deep convolutional autoencoder

We provide a detailed architecture of the generator used in this study in Table C.1. In Table C.1, B is batch size, C is input channel, and we set $C = 1$ throughout this study. Furthermore, we note that we typically employ unstructured grids in the finite element solver or FOM presented in Appendix A. In contrast, DC-AE is usually employed on a structured data set. Thus, we pre-process our snapshot data by interpolating the finite element result T_h to structured grids, such as the finite element interpolation operator or cubic spline interpolation. We then replace the FOM dimension N_h^T , associated with the unstructured grid, with a pair $(\tilde{N}_h^T, \tilde{N}_h^T)$, associated to the structured grid. In practice, the value of \tilde{N}_h^T is often chosen independently on N_h^T .

The 1st convolutional layer is used to map C to hidden layer size (H), and it does not subject to any activation function. We note that we set $H = 32$ throughout this work. The 2nd convolutional layer is used to map hidden layer size (H) back to C , and it subjects to the Sigmoid activation function as our data $T_h(\mu^{(1)}), \dots, T_h(\mu^{(M)})$ is normalized to be in a range of $[0, 1]$ as follows

$$\frac{T_h(\cdot; t^k, \mu^i) - \min(T_h)}{\max(T_h) - \min(T_h)}. \quad (\text{C.18})$$

Table C.1: Deep convolutional autoencoder used in this study (input and output sizes are represented by [B, C, \tilde{N}_h^T , \tilde{N}_h^T]. We use hidden layers H = 32.)

block	input size	output size	batch normalization	dropout
1 st convolutional layer	[B, 1, 128, 128]	[B, 32, 128, 128]		
1 st contracting block	[B, 32, 128, 128]	[B, 64, 64, 64]	✓	✓
2 nd contracting block	[B, 64, 64, 64]	[B, 128, 32, 32]	✓	✓
3 rd contracting block	[B, 128, 32, 32]	[B, 256, 16, 16]	✓	✓
4 th contracting block	[B, 256, 16, 16]	[B, 512, 8, 8]	✓	
5 th contracting block	[B, 512, 8, 8]	[B, 1024, 4, 4]	✓	
6 th contracting block	[B, 1024, 4, 4]	[B, 2048, 2, 2]	✓	
7 th contracting block	[B, 2048, 2, 2]	[B, 4196, 1, 1]	✓	
1 st bottleneck	reshape([B, 4196])	[B, z]		
2 nd bottleneck	[B, z]	reshape([B, 4196])		
1 st expanding block	[B, 4196, 1, 1]	[B, 2048, 2, 2]	✓	
2 nd expanding block	[B, 2048, 2, 2]	[B, 1024, 4, 4]	✓	
3 rd expanding block	[B, 1024, 4, 4]	[B, 512, 8, 8]	✓	
4 th expanding block	[B, 512, 8, 8]	[B, 256, 16, 16]	✓	
5 th expanding block	[B, 256, 16, 16]	[B, 128, 32, 32]	✓	
6 th expanding block	[B, 128, 32, 32]	[B, 64, 64, 64]	✓	
7 th expanding block	[B, 64, 64, 64]	[B, 32, 128, 128]	✓	
2 nd convolutional layer	[B, 32, 128, 128]	[B, 1, 128, 128]		

Appendix D Information on training losses of approximators

We present supplementary information on training losses of the approximators used for the nonlinear compression approach (see Section 3.2). Figure D.1 contains RBF loss information for Example 1, Figure D.2 contains RBF loss information for Example 2, and Figure D.3 provides ANN validation loss during the training phase for Examples 1, 2, and 3.

From Figure D.1, we observe that the RBF with linear function has an extremely low loss (in an order of 10^{-20}). The RBF models with cubic function have a higher loss, but still, they are pretty low (in order of 10^{-10}). The similar results hold for Example 2 - see Figure D.2. The validation loss shown in Figure D.3 is decreased as a function of epoch. We observe that the values of validation loss are not much different between each Q for each example.

Appendix E Example 2: Elder problem using autoencoder without convolutional layers

Here, we provide MSE and max(DIFF) results of Example 2 using an autoencoder without convolutional layers. The results are presented in Figure E.4. We note that our autoencoder here utilizes seven linear hidden layers for its encoder as well as seven linear hidden layers for its decoder. Each hidden layer is subjected to *tanh* activation function. Comparing to Figure 11, it is clear that the models without convolutional layers have less accuracy than the ones that have. However, the autoencoder without convolutional layers still outperforms the linear compression approach for this Example 2.

References

- J. Taron and D. Elsworth. Thermal-hydrologic-mechanical-chemical processes in the evolution of engineered geothermal reservoirs. *International Journal of Rock Mechanics and Mining Sciences*, 46(5):855–864, 2009.
- H. Nick, A. Raoof, F. Centler, M. Thullner, and P. Regnier. Reactive dispersive contaminant transport in coastal aquifers: numerical simulation of a reactive henry problem. *Journal of contaminant hydrology*, 145:90–104, 2013.
- C. Zheng and G. Bennett. *Applied contaminant transport modeling*, volume 2. Wiley-Interscience New York, 2002.
- J. Rutqvist, M. Chijimatsu, L. Jing, A. Millard, T. Nguyen, A. Rejeb, Y. Sugita, and C. Tsang. A numerical study of THM effects on the near-field safety of a hypothetical nuclear waste repository—BMT1 of the DECOVALEX III project. part 3: Effects of THM coupling in sparsely fractured rocks. *International Journal of Rock Mechanics and Mining Sciences*, 42(5-6):745–755, 2005.

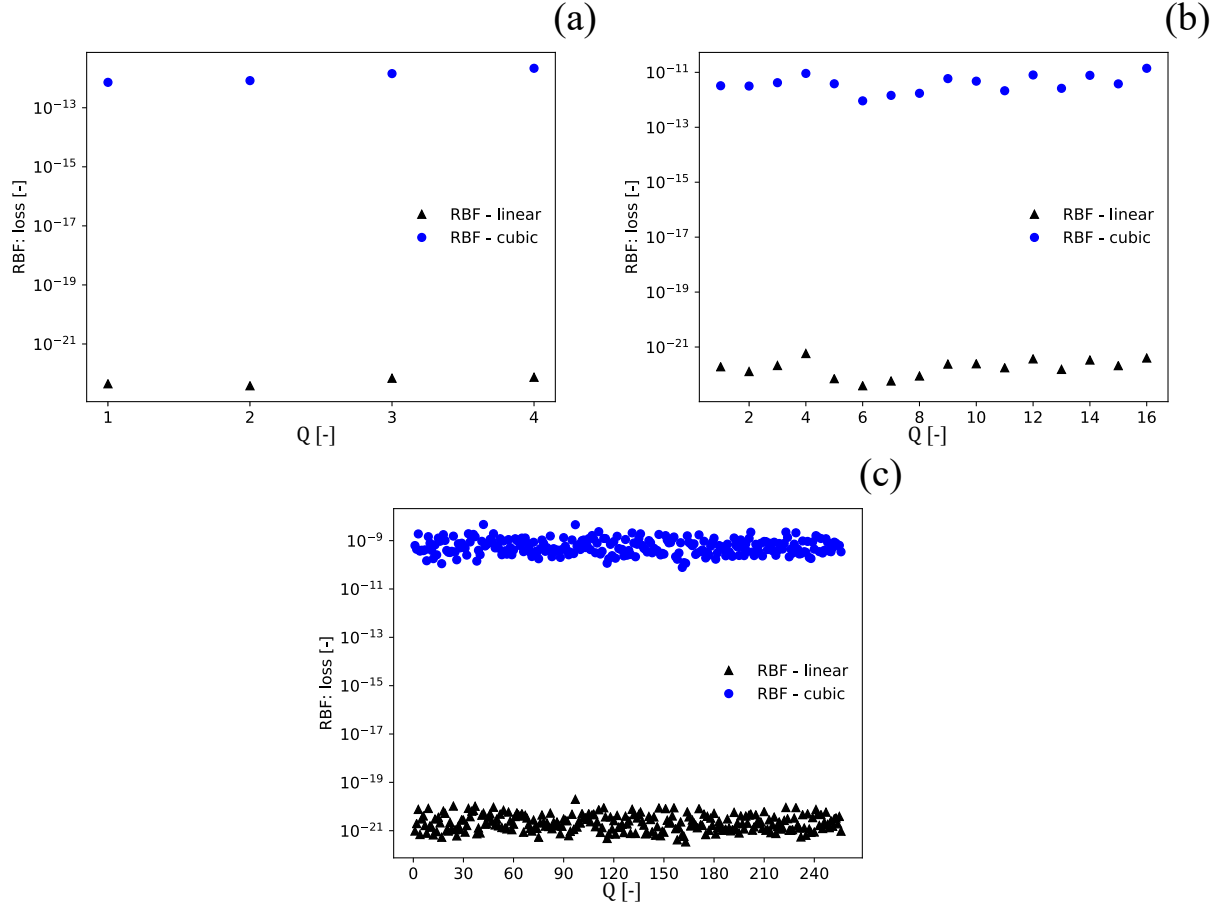


Figure D.1: RBF: loss for nonlinear compression approach of Example 1: (a) $Q = 4$, (b) $Q = 16$, and (c) $Q = 256$.

D. Nield and A. Bejan. *Convection in porous media*, volume 3. Springer, 2006.

H. Hassanzadeh, M. Pooladi-Darvish, and D. Keith. Scaling behavior of convective mixing, with application to geological storage of CO₂. *AIChE journal*, 53(5):1121–1131, 2007.

J. Neufeld, M. Hesse, A. Riaz, M. Hallworth, H. A Tchelepi, and H. Huppert. Convective dissolution of carbon dioxide in saline aquifers. *Geophysical research letters*, 37(22), 2010.

T. Kadeethum, S. Lee, F. Ballarin, J. Choo, and H. Nick. A locally conservative mixed finite element framework for coupled hydro-mechanical-chemical processes in heterogeneous porous media. *Computers & Geosciences*, page 104774, 2021a.

C. Zhang, S. Zarrouk, and R. Archer. A mixed finite element solver for natural convection in porous media using automated solution techniques. *Computers & Geosciences*, 96:181–192, 2016.

N. Hosseini, Z. Bajalan, and A. Khoei. Numerical modeling of density-driven solute transport in fractured porous media with the extended finite element method. *Advances in Water Resources*, 136:103453, 2020.

H. Diersch. Finite element modelling of recirculating density-driven saltwater intrusion processes in groundwater. *Advances in Water Resources*, 11(1):25–43, 1988.

P. Frolkovič and H. De Schepper. Numerical modelling of convection dominated transport coupled with density driven flow in porous media. *Advances in Water Resources*, 24(1):63–72, 2000.

K. Cheng and A. Rabinovich. Upscaling capillary pressure curves for numerical modeling of gravity-capillary driven flow. *Advances in Water Resources*, 142:103639, 2020.

O. Kolditz, R. Ratke, H. Diersch, and W. Zielke. Coupled groundwater flow and transport: 1. verification of variable density flow and transport models. *Advances in water resources*, 21(1):27–46, 1998.

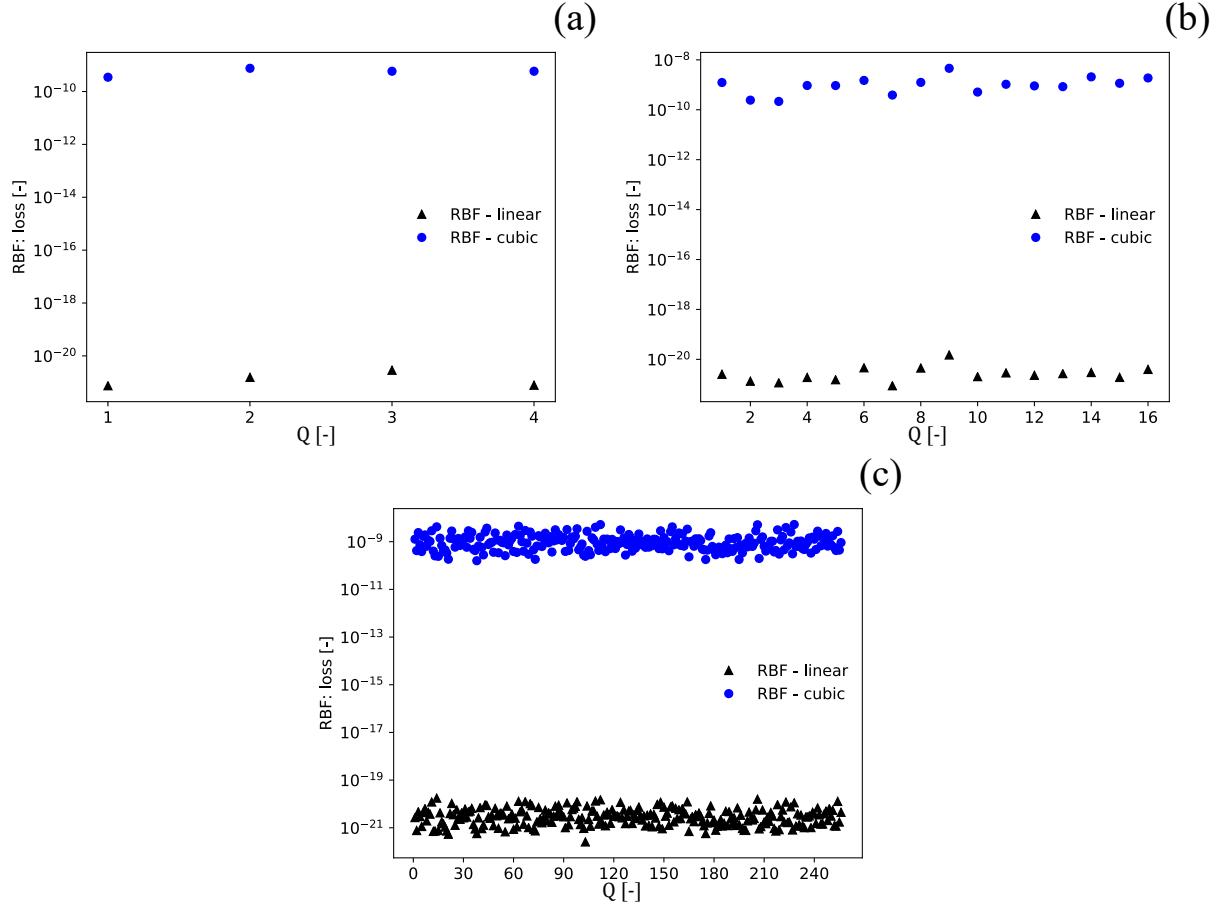


Figure D.2: RBF: loss for nonlinear compression approach of Example 2: (a) $Q = 4$, (b) $Q = 16$, and (c) $Q = 256$.

David Amsallem, Matthew Zahr, Youngsoo Choi, and Charbel Farhat. Design optimization using hyper-reduced-order models. *Structural and Multidisciplinary Optimization*, 51(4):919–940, 2015.

Sean McBane and Youngsoo Choi. Component-wise reduced order model lattice-type structure design. *Computer Methods in Applied Mechanics and Engineering*, 381:113813, 2021.

Youngsoo Choi, Geoffrey Oxberry, Daniel White, and Trenton Kirchdoerfer. Accelerating design optimization using reduced order models. *arXiv preprint arXiv:1909.11320*, 2019a.

Youngsoo Choi, Gabriele Boncoraglio, Spenser Anderson, David Amsallem, and Charbel Farhat. Gradient-based constrained optimization using a database of linear reduced-order models. *Journal of Computational Physics*, 423: 109787, 2020a.

F. Ballarin, A. D’amario, S. Perotto, and G. Rozza. A POD-selective inverse distance weighting method for fast parametrized shape morphing. *International Journal for Numerical Methods in Engineering*, 117(8):860–884, 2019.

P. Hansen. *Discrete inverse problems: insight and algorithms*, volume 7. Siam, 2010.

J. Hesthaven, G. Rozza, and B. Stamm. *Certified reduced basis methods for parametrized partial differential equations*. Springer, 2016.

W. Schilders, H. Van der Vorst, and J. Rommes. *Model order reduction: theory, research aspects and applications*, volume 13. Springer, 2008.

W. Schilders. Introduction to model order reduction. In *Model order reduction: Theory, research aspects and applications*, pages 3–32. Springer, 2008.

Dylan Matthew Copeland, Siu Wun Cheung, Kevin Huynh, and Youngsoo Choi. Reduced order models for lagrangian hydrodynamics. *arXiv preprint arXiv:2104.11404*, 2021.

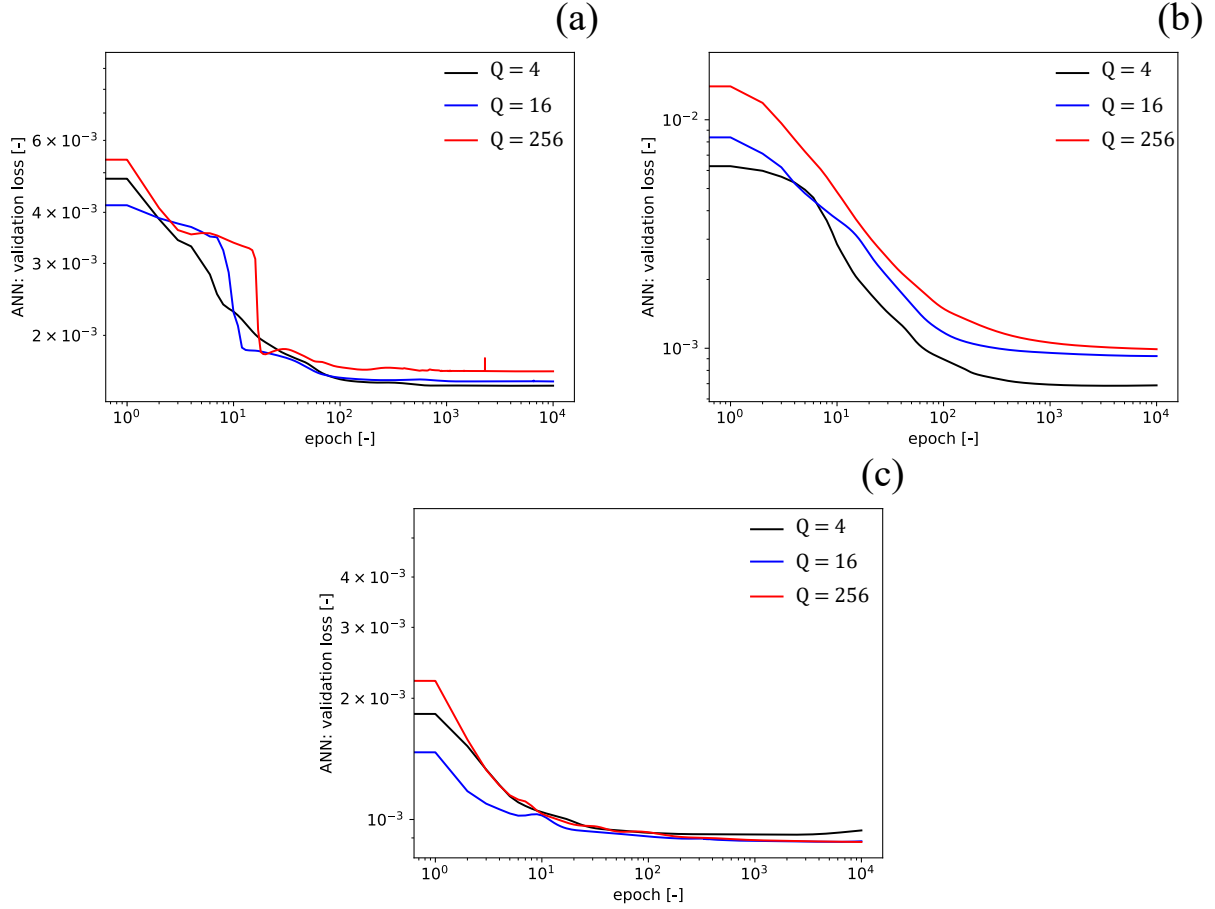


Figure D.3: ANN: validation loss for nonlinear compression approach of (a) Example 1, (b) Example 2, and (c) Example 3.

Chi Hoang, Youngsoo Choi, and Kevin Carlberg. Domain-decomposition least-squares petrov-galerkin (dd-lspg) nonlinear model reduction. *arXiv preprint arXiv:2007.11835*, 2020.

Youngkyu Kim, Karen May Wang, and Youngsoo Choi. Efficient space-time reduced order model for linear dynamical systems in python using less than 120 lines of code. *arXiv preprint arXiv:2011.10648*, 2020a.

Youngsoo Choi, Deshawn Coombs, and Robert Anderson. Sns: a solution-based nonlinear subspace method for time-dependent model order reduction. *SIAM Journal on Scientific Computing*, 42(2):A1116–A1146, 2020b.

Youngsoo Choi and Kevin Carlberg. Space-time least-squares petrov-galerkin projection for nonlinear model reduction. *SIAM Journal on Scientific Computing*, 41(1):A26–A58, 2019.

Youngsoo Choi, Peter Brown, William Arrighi, Robert Anderson, and Kevin Huynh. Space-time reduced order model for large-scale linear dynamical systems with application to boltzmann transport problems. *Journal of Computational Physics*, 424:109845, 2021.

Kevin Carlberg, Youngsoo Choi, and Syuzanna Sargsyan. Conservative model reduction for finite-volume models. *Journal of Computational Physics*, 371:280–314, 2018.

L. Venturi, F. Ballarin, and G. Rozza. A weighted POD method for elliptic PDEs with random inputs. *Journal of Scientific Computing*, 81(1):136–153, 2019.

V. DeCaria, T. Iliescu, W. Layton, M. McLaughlin, and M. Schneier. An artificial compression reduced order model. *SIAM Journal on Numerical Analysis*, 58(1):565–589, 2020.

J. Cleary and I. Witten. Data compression using adaptive coding and partial string matching. *IEEE transactions on Communications*, 32(4):396–402, 1984.

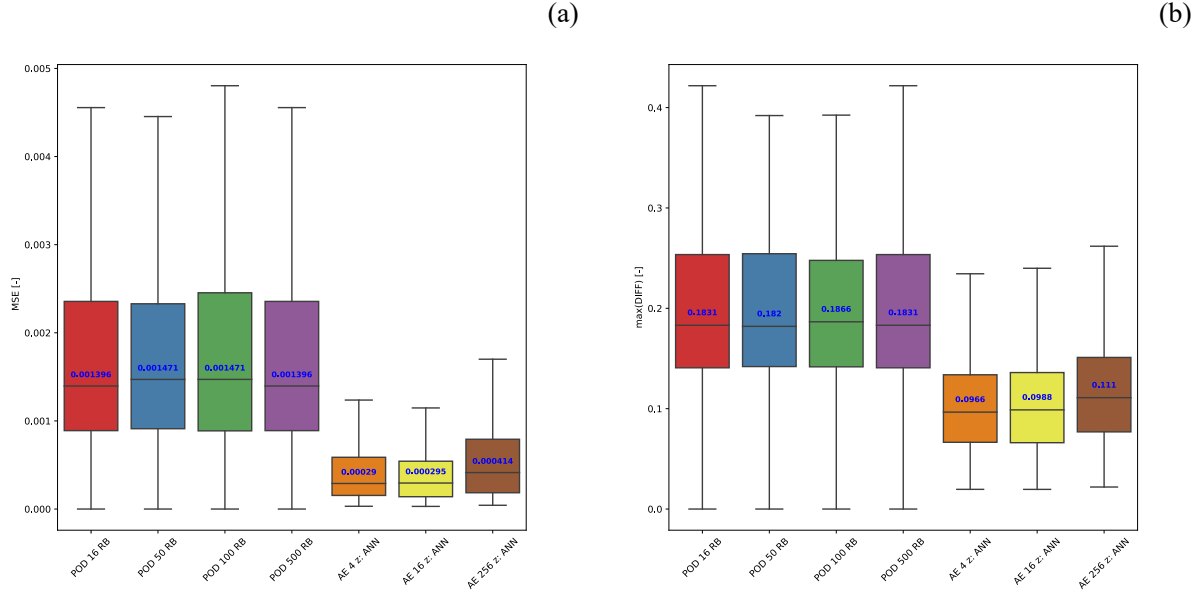


Figure E.4: Example 2 - without convolutional layers: Each model's performance on a test set (a) mean square error (MSE) and (b) maximum DIFF (max(DIFF)). Blue text represents a mean value. 16 RB, 50 RB, 100 RB, and 500 RB represent linear compression models with $[N_{\text{int}} = 16, N = 16]$, $[N_{\text{int}} = 50, N = 50]$, $[N_{\text{int}} = 100, N = 100]$, and $[N_{\text{int}} = 500, N = 500]$, respectively.

S. Hijazi, S. Ali, G. Stabile, F. Ballarin, and G. Rozza. The effort of increasing Reynolds number in projection-based reduced order methods: from laminar to turbulent flows. In *Numerical Methods for Flows*, pages 245–264. Springer, 2020.

Chi Hoang, Kenny Chowdhary, Kookjin Lee, and Jaideep Ray. *arXiv preprint arXiv:2102.03505*, 2021.

Xuping Xie, Guannan Zhang, and Clayton G Webster. Non-intrusive inference reduced order model for fluids using deep multistep neural network. *Mathematics*, 7(8):757, 2019.

D. Xiao, C. Heaney, F. Fang, L. Mottet, R. Hu, D Bistrain, E. Aristodemou, I. Navon, and C. Pain. A domain decomposition non-intrusive reduced order model for turbulent flows. *Computers & Fluids*, 182:15–27, 2019.

J. Hesthaven and S. Ubbiali. Non-intrusive reduced order modeling of nonlinear problems using neural networks. *Journal of Computational Physics*, 363:55–78, 2018.

M. Mignolet, A. Przekop, S. Rizzi, and M. Spottswood. A review of indirect/non-intrusive reduced order modeling of nonlinear geometric structures. *Journal of Sound and Vibration*, 332(10):2437–2460, 2013.

D. Xiao, F. Fang, C. Pain, and G. Hu. Non-intrusive reduced-order modelling of the Navier–Stokes equations based on rbf interpolation. *International Journal for Numerical Methods in Fluids*, 79(11):580–595, 2015.

M. Girfoglio, L. Scandurra, F. Ballarin, G. Infantino, F. Nicolò, A. Montalto, G. Rozza, R. Scrofani, M. Comisso, and F. Musumeci. A non-intrusive data-driven ROM framework for hemodynamics problems. *arXiv preprint arXiv:2010.08139*, 2020.

G. Ortali, N. Demo, and G. Rozza. Gaussian process approach within a data-driven POD framework for fluid dynamics engineering problems. *arXiv preprint arXiv:2012.01989*, 2020.

N. Demo, G. Ortali, G. Gustin, G. Rozza, and G. Lavini. An efficient computational framework for naval shape design and optimization problems by means of data-driven reduced order modeling techniques. *arXiv preprint arXiv:2004.11201*, 2020.

M. Gadalla, M. Cianferra, M. Tezzele, G. Stabile, A. Mola, and G. Rozza. On the comparison of LES data-driven reduced order approaches for hydroacoustic analysis. *arXiv preprint arXiv:2006.14428*, 2020.

Teeratrorn Kadeethum, Francesco Ballarin, and Nikolaos Bouklas. Data-driven reduced order modeling of poroelasticity of heterogeneous media based on a discontinuous galerkin approximation. *GEM-International Journal on Geomathematics*, 12(1):1–45, 2021b.

- Youngkyu Kim, Youngsoo Choi, David Widemann, and Tarek Zohdi. A fast and accurate physics-informed neural network reduced order model with shallow masked autoencoder. *arXiv preprint arXiv:2009.11990*, 2020b.
- Youngkyu Kim, Youngsoo Choi, David Widemann, and Tarek Zohdi. Efficient nonlinear manifold reduced order model. *arXiv preprint arXiv:2011.07727*, 2020c.
- T. Phillips, C. Heaney, P. Smith, and C. Pain. An autoencoder-based reduced-order model for eigenvalue problems with application to neutron diffusion. *arXiv preprint arXiv:2008.10532*, 2020.
- S. Nikolopoulos, I. Kalogeris, and V. Papadopoulos. Non-intrusive surrogate modeling for parametrized time-dependent PDEs using convolutional autoencoders. *arXiv preprint arXiv:2101.05555*, 2021.
- K. Lee and K. Carlberg. Model reduction of dynamical systems on nonlinear manifolds using deep convolutional autoencoders. *Journal of Computational Physics*, 404:108973, 2020.
- S. Fresca, L. Dede, and A. Manzoni. A comprehensive deep learning-based approach to reduced order modeling of nonlinear time-dependent parametrized pdes. *Journal of Scientific Computing*, 87(2):1–36, 2021.
- D. Joseph. *Stability of fluid motions I*, volume 27. Springer Science & Business Media, 2013.
- Z. Chen, G. Huan, and Y. Ma. *Computational methods for multiphase flows in porous media*, volume 2. Siam, 2006.
- L. Lake, R. Johns, B. Rossen, and G. Pope. *Fundamentals of enhanced oil recovery*. Society of Petroleum Engineers Richardson, TX, 2014.
- A. Paul-Dubois-Taine and D. Amsallem. An adaptive and efficient greedy procedure for the optimal training of parametric reduced-order models. *International Journal for Numerical Methods in Engineering*, 102(5):1262–1292, 2015.
- M. Vasile, E. Minisci, D. Quagliarella, M. Guénot, I. Lepot, C. Sainvitu, J. Goblet, and R. Coelho. Adaptive sampling strategies for non-intrusive pod-based surrogates. *Engineering computations*, 2013.
- K. Willcox and J. Peraire. Balanced model reduction via the proper orthogonal decomposition. *AIAA journal*, 40(11):2323–2330, 2002.
- A. Chatterjee. An introduction to the proper orthogonal decomposition. *Current science*, pages 808–817, 2000.
- Y. Liang, H. Lee, S. Lim, W. Lin, K. Lee, and C. Wu. Proper orthogonal decomposition and its applications—part i: Theory. *Journal of Sound and vibration*, 252(3):527–544, 2002.
- Z. Wang, D. Xiao, F. Fang, R. Govindan, C. Pain, and Y. Guo. Model identification of reduced order fluid dynamics systems using deep learning. *International Journal for Numerical Methods in Fluids*, 86(4):255–268, 2018.
- J. Romero, J. Olson, and A. Aspuru-Guzik. Quantum autoencoders for efficient compression of quantum data. *Quantum Science and Technology*, 2(4):045001, 2017.
- P. Baldi. Autoencoders, unsupervised learning, and deep architectures. In *Proceedings of ICML workshop on unsupervised and transfer learning*, pages 37–49, 2012.
- G. Hinton and R. Zemel. Autoencoders, minimum description length and Helmholtz free energy. In *Advances in neural information processing systems*, pages 3–10, 1994.
- D. O’Malley, J. Golden, and V. Vesselinov. Learning to regularize with a variational autoencoder for hydrologic inverse analysis. *arXiv preprint arXiv:1906.02401*, 2019.
- H. Goh, S. Sherifdeen, and T. Bui-Thanh. Solving forward and inverse problems using autoencoders. *arXiv preprint arXiv:1912.04212*, 2019.
- J. Gehring, Y. Miao, F. Metze, and A. Waibel. Extracting deep bottleneck features using stacked auto-encoders. In *2013 IEEE international conference on acoustics, speech and signal processing*, pages 3377–3381. IEEE, 2013.
- C. Audouze, F. De Vuyst, and P. B. Nair. Reduced-order modeling of parameterized PDEs using time-space-parameter principal component analysis. *International Journal for Numerical Methods in Engineering*, 80(8):1025–1057, 2009.
- María-Luisa Rapún and José M Vega. Reduced order models based on local POD plus Galerkin projection. *Journal of Computational Physics*, 229(8):3046–3063, 2010.
- Christophe Audouze, Florian De Vuyst, and Prasanth B. Nair. Nonintrusive reduced-order modeling of parametrized time-dependent partial differential equations. *Numerical Methods for Partial Differential Equations*, 29(5):1587–1628, 2013.
- Francesco Ballarin, Elena Faggiano, Sonia Ippolito, Andrea Manzoni, Alfio Quarteroni, Gianluigi Rozza, and Roberto Scrofani. Fast simulations of patient-specific haemodynamics of coronary artery bypass grafts based on a POD–Galerkin method and a vascular shape parametrization. *Journal of Computational Physics*, 315:609–628, 2016.

- Christian Himpe, Tobias Leibner, and Stephan Rave. Hierarchical approximate proper orthogonal decomposition. *SIAM Journal on Scientific Computing*, 40(5):A3267–A3292, 2018.
- Q. Wang, J. Hesthaven, and D. Ray. Non-intrusive reduced order modeling of unsteady flows using artificial neural networks with application to a combustion problem. *Journal of computational physics*, 384:289–307, 2019.
- P. Jacquier, A. Abdedou, V. Delmas, and A. Soulaïmani. Non-intrusive reduced-order modeling using uncertainty-aware deep neural networks and proper orthogonal decomposition: Application to flood modeling. *arXiv preprint arXiv:2005.13506*, 2020.
- A. Paszke, S. Gross, F. Massa, A. Lerer, J. Bradbury, Gregory Chanan, Trevor Killeen, Zeming Lin, Natalia Gimelshein, Luca Antiga, Alban Desmaison, Andreas Kopf, Edward Yang, Zachary DeVito, Martin Raison, Alykhan Tejani, Sasank Chilamkurthy, Benoit Steiner, Lu Fang, Junjie Bai, and Soumith Chintala. Pytorch: An imperative style, high-performance deep learning library. In H. Wallach, H. Larochelle, A. Beygelzimer, F. d'Alché-Buc, E. Fox, and R. Garnett, editors, *Advances in Neural Information Processing Systems 32*, pages 8024–8035. Curran Associates, Inc., 2019. URL <http://papers.neurips.cc/paper/9015-pytorch-an-imperative-style-high-performance-deep-learning-library.pdf>.
- D. Kingma and J. Ba. Adam: A method for stochastic optimization. *arXiv preprint arXiv:1412.6980*, 2014.
- L. Prechelt. Early stopping-but when? In *Neural Networks: Tricks of the trade*, pages 55–69. Springer, 1998a.
- L. Prechelt. Automatic early stopping using cross validation: quantifying the criteria. *Neural Networks*, 11(4):761–767, 1998b.
- P. Vincent, H. Larochelle, Y. Bengio, and P. Manzagol. Extracting and composing robust features with denoising autoencoders. In *Proceedings of the 25th international conference on Machine learning*, pages 1096–1103, 2008.
- T. Kadeethum, D. O'Malley, J. Fuhg, Y. Choi, J. Lee, H. Viswanathan, and N. Bouklas. A framework for data-driven solution and parameter estimation of pdes using conditional generative adversarial networks. *arXiv preprint arXiv:2105.13136*, 2021c.
- I. Loshchilov and F. Hutter. Sgdr: Stochastic gradient descent with warm restarts. *arXiv preprint arXiv:1608.03983*, 2016.
- G. Wright. *Radial basis function interpolation: numerical and analytical developments*. University of Colorado at Boulder, 2003.
- E. Jones, T. Oliphant, P. Peterson, and Others. SciPy: Open source scientific tools for Python, 2001. URL <http://www.scipy.org/>.
- J. Elder. Transient convection in a porous medium. *Journal of Fluid Mechanics*, 27(3):609–623, 1967.
- M. Simpson and T. Clement. Theoretical analysis of the worthiness of Henry and Elder problems as benchmarks of density-dependent groundwater flow models. *Advances in Water Resources*, 26(1):17–31, 2003.
- H. Diersch and O. Kolditz. Variable-density flow and transport in porous media: approaches and challenges. *Advances in water resources*, 25(8-12):899–944, 2002.
- T. Kipf and M. Welling. Semi-supervised classification with graph convolutional networks. *arXiv preprint arXiv:1609.02907*, 2016.
- C. Heaney, Y. Li, O. Matar, and C. Pain. Applying convolutional neural networks to data on unstructured meshes with space-filling curves. *arXiv preprint arXiv:2011.14820*, 2020.
- Y. Choi, W. Arrighi, D. Copeland, R. Anderson, and G. Oxberry. librom. Technical report, Lawrence Livermore National Lab.(LLNL), Livermore, CA (United States), 2019b.
- H. Abdi and L. Williams. Principal component analysis. *Wiley interdisciplinary reviews: computational statistics*, 2(4):433–459, 2010.
- L. Van der Maaten and G. Hinton. Visualizing data using t-SNE. *Journal of machine learning research*, 9(11), 2008.
- R. Courant, K. Friedrichs, and H. Lewy. On the partial difference equations of mathematical physics. *IBM journal of Research and Development*, 11(2):215–234, 1967.
- Z. Ibrahim, K. Othman, and M. Suleiman. Implicit r-point block backward differentiation formula for solving first-order stiff ODEs. *Applied Mathematics and Computation*, 186(1):558–565, 2007.
- O. Akinfenwa, S. Jator, and N. Yao. Continuous block backward differentiation formula for solving stiff ordinary differential equations. *Computers & Mathematics with Applications*, 65(7):996–1005, 2013.
- S. Lee, A. Mikelic, M. Wheeler, and T. Wick. Phase-field modeling of two phase fluid filled fractures in a poroelastic medium. *Multiscale Modeling & Simulation*, 16(4):1542–1580, 2018.

- F. Brezzi and M. Fortin. *Mixed and hybrid finite element methods*, volume 15. Springer Science & Business Media, 2012.
- S. Lee, Y. Lee, and M. Wheeler. A locally conservative enriched Galerkin approximation and efficient solver for elliptic and parabolic problems. *SIAM Journal on Scientific Computing*, 38(3):A1404–A1429, 2016.
- S. Sun and J. Liu. A locally conservative finite element method based on piecewise constant enrichment of the continuous Galerkin method. *SIAM Journal on Scientific Computing*, 31(4):2528–2548, 2009.
- B. Riviere. *Discontinuous Galerkin methods for solving elliptic and parabolic equations: theory and implementation*. SIAM, 2008.
- B. Riviere and M. Wheeler. A discontinuous Galerkin method applied to nonlinear parabolic equations. In *Discontinuous Galerkin methods*, pages 231–244. Springer, 2000.